Low-Overhead Kronecker-Based Intelligent Reflective Surfaces for Next-Generation Wireless Networks

by

Inshi Nimnadini

A Thesis submitted to The Faculty of Graduate Studies of

The University of Manitoba

in partial fulfillment of the requirements for the degree of

Master of Science

Department of Electrical and Computer Engineering

University of Manitoba

Winnipeg

February 2025

You will never reach your destination if you stop and throw stones at every dog that barks.

Winston Churchill

Abstract

This thesis investigates the optimization of Intelligent Reflective Surfaces (IRSs) in wireless communication networks, focusing on reducing control overhead and enhancing network performance. A key contribution of this work is the introduction of a Kronecker-based phase shift model, which significantly reduces the overhead required for controlling the phase shifts of the IRSs. By representing the phase shifts of each IRS with fewer control signals, this approach simplifies the wiring systems in IRSs and enables faster switching between configurations. The research initially focuses on a downlink transmission system, formulating an optimization problem based on the minimum mean square error (MMSE) criterion. This results in a multi-variable non-convex problem, which is then tackled using alternating optimization (AO). The Kronecker-based method is shown to outperform traditional phase shift control in terms of efficiency and scalability.

The thesis then extends this model to cell-free multiple-input multiple-output (MIMO) systems, incorporating multiple IRSs to enhance coverage, mitigate interference, and improve performance. Here, optimization frameworks for uplink and downlink communication are developed, focusing on joint optimization of IRS phase shifts and beamforming/receiver matrices at distributed base stations (BSs). The performance is evaluated using sum-rate and good-put metrics, with numerical simulations demonstrating that the proposed approach reduces control overhead while improving system performance in large-scale environments. The results highlight the potential of the Kronecker-based method for efficient IRS deployment in future wireless networks.

Keywords: Intelligent Reflective Surface (IRS), Kronecker-based phase shift matrix, cell-free MIMO systems

Acknowledgement

First, I would like to express my deepest gratitude to my supervisor, Professor Ekram Hossain, for his invaluable guidance throughout this program. It has been an honor to learn and grow under his expert mentorship, and I am truly appreciative of the support and wisdom he has shared.

I would also like to extend my heartfelt thanks to Professor Amine Mezghani for his insightful guidance and meaningful contributions throughout this journey. It has been a privilege to work under his supervision, and I deeply appreciate the knowledge and personal growth I have gained through his mentorship.

Additionally, I am sincerely grateful to my committee members, Professor Pradeepa Yahampath and Professor Amine Mezghani, for their constructive feedback that has greatly enhanced the quality of this work.

Finally, I wish to express my deepest gratitude to my family for their unwavering belief in me and their constant encouragement through every challenge and success. I am also incredibly thankful to my friends for their support and companionship along the way.

Table of Contents

List of Figures

List of Tables

Contribution of Authors

The thesis follows a "sandwich" or grouped-manuscript format, with Chapters 2 and 3 incorporating content from a published conference paper and a journal article currently under review, respectively. Below are the titles of these research articles, their review status at the time of thesis submission, the contributions of the authors, and the corresponding thesis chapters.

1. Chapter 2 includes the content of the conference paper titled "Low-Overhead Kronecker-Based Intelligent Reflective Surfaces for 5G and Beyond" which was published in IEEE World Forum on Internet of Things held on 10 - 13 November 2024. DOI: 0.1109/WF-IoT62078.2024.10811391.

   Author contributions:

   I. Nimnadini (*Thesis Author*): Concept development, Methodology design, Analysis and optimization, Simulation and validation, Manuscript preparation.

   A. Mezghani: Concept development, Methodology design, Supervision, Manuscript review and editing.

   E. Hossain: Concept development, Supervision, Manuscript review and editing.

2. Chapter 3 contains the content of the journal paper titled "Cell-Free MIMO Systems Enhanced With Kronecker-Based Intelligent Reflective Surfaces", which is submitted to IEEE Transactions on Wireless Communications on 31 December 2024, and is under review at the date of thesis submission.

   Author contributions:

   I. Nimnadini (*Thesis Author*): Concept development, Methodology design, Analysis and optimization, Simulation and validation, Manuscript preparation.

   A. Mezghani: Concept development, Methodology design, Supervision, Manuscript review and editing.

   E. Hossain: Concept development, Supervision, Manuscript review and editing.

List of Abbreviations

IRS	Intelligent Reflective Surface
MMSE	Minimum Mean Square Error
AO	Alternating Optimization
MIMO	Multiple Input Multiple Output
BS	Base Station
mmWave	millimeter-wave
LTE	Long-Term Evolution
AP	Access Point
UE	User Equipment
CPU	Central Processing Unit
EM	Electromagnetic
MEMS	Micro-Electro-Mechanical System
SINR	Signal-to-interference-plus-noise ratio
CSI	Channel State Information
UPA	Uniform Planar Array
AWGN	Additive White Gaussian Noise
MSE	Mean Square Error
SNR	Signal-to-noise ratio
LMMSE	Linear Minimum Mean Square Error

SIM	Stacked Intelligent Metasurface

Chapter 1

Introduction

1.1 Overview

Wireless networks are a key part of modern communication, allowing data to be sent without the need for physical connections [1]. Recent advancements in wireless communication have been driven by the increasing demand for faster, more reliable, and energy-efficient connectivity across various industries [2,3]. The launch of 5G technology has been a game-changer, offering ultra-low latency, faster data rates, and the ability to connect a massive number of devices simultaneously [4–6]. These 5G networks are expected to enable a wide range of innovations, from autonomous vehicles [7] to remote healthcare [8] and smart cities [9]. One of the key innovations within 5G is the deployment of millimeter-wave (mmWave) frequencies, which provide greater bandwidth and higher speeds, but also come with challenges related to signal attenuation [4, 10]. To address this, advanced MIMO technology is being utilized to improve the capacity of networks by transmitting multiple signals simultaneously from both BSs and user devices, enhancing data throughput while reducing congestion in densely populated areas [11].

In addition to the improvements brought by 5G, advancements in network architecture are driving the shift towards cell-free networks. Unlike traditional cellular networks where coverage is provided by a limited number of BSs, cell-free networks distribute BSs across a wide area to offer uniform coverage and enhanced reliability [12]. In these networks, effective coordination between distributed antennas and users is crucial, and techniques such as coordinated beamforming and network densification are employed to enhance communication efficiency [13]. This approach has the potential to significantly improve both signal strength and user experience, especially in dense urban environments where traditional cellular networks often struggle with coverage [14, 15].

Furthermore, the concept of IRSs has emerged as a promising solution to boost network performance. IRSs consist of large arrays of low-cost, passive reflective elements that can control the propagation of radio waves without the need for active transmitters [16]. By adjusting the phase of the reflected signals, IRSs can direct them toward the intended receiver, enhancing signal strength, coverage, and energy efficiency [17–19]. This technology has shown significant potential in improving the performance of wireless networks, particularly in complex environments with challenging propagation conditions [20, 21]. The integration of IRSs into both cell-based and cell-free systems enables the reduction of interference, as the reflective surfaces can intelligently redirect signals, mitigating issues like blockage and fading that are often encountered in traditional systems [21–23].

As these technologies continue to evolve, the focus is also shifting toward sustainability and energy efficiency. Green wireless communication technologies, including energy-efficient protocols and network designs, are becoming more critical to reduce the environmental impact of expanding wireless infrastructures [24, 25]. Researchers are exploring solutions such as energy harvesting, where wireless devices can recharge themselves using ambient energy from radio signals or solar power, contributing to the overall sustainability of wireless systems [26, 27].

1.2 Cell-Based Networks vs. Cell-Free and Cell-Free MIMO Networks

Wireless networks have traditionally been designed based on a cellular structure, where a geographical area is divided into smaller regions called cells, each served by a dedicated BS. This architecture, commonly referred to as a cell-based network, has been the foundation of mobile communication systems from the early generations (1G, 2G) to modern 4G Long-Term Evolution (LTE) and 5G networks [28].

However, as wireless communication demands continue to increase, conventional cell-based architectures face significant challenges such as inter-cell interference, coverage gaps, and mobility-induced handovers. To address these limitations, a new concept called cell-free networks has emerged, where a large number of distributed access points (APs) or BSs jointly serve all users in a coordinated manner [12]. Unlike traditional cell-based systems, cell-free networks eliminate cell boundaries, offering seamless connectivity and improved spectral efficiency [29]. Furthermore, this concept is extended to cell-free MIMO networks, where MIMO technology is integrated to significantly enhance the performance of communication systems, improving data rates, capacity, and interference management [30–32].

1.2.1 Cell-Based Networks: Principles and Limitations

In traditional cell-based networks, each BS is responsible for a designated coverage area, commonly referred to as a cell, as illustrated in Fig. 1.1. Within each cell, users establish communication exclusively with their serving BS, ensuring localized connectivity and efficient network operation. However, when a user moves beyond the boundaries of its assigned cell, a handover process becomes necessary to transfer the ongoing connection to a new BS in the adjacent cell. This handover mechanism ensures seamless connectiv-

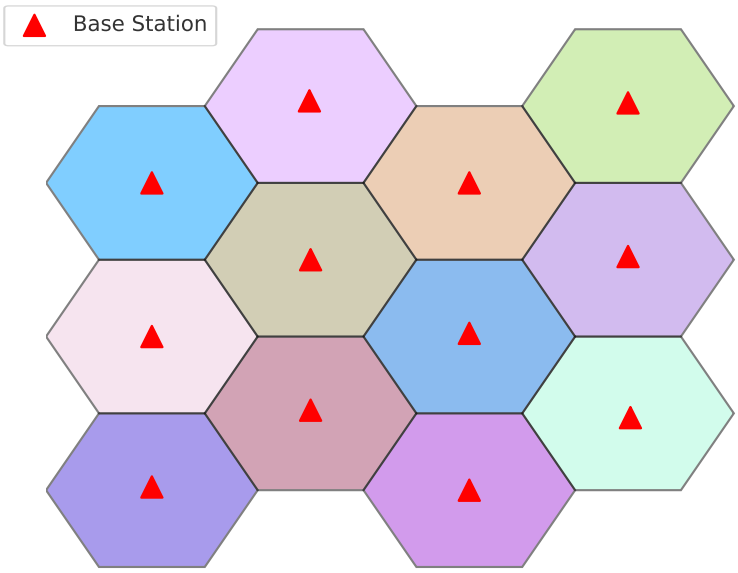

Figure 1.1: Cell-based network architecture

ity but can introduce latency, signaling overhead, and potential service interruptions, particularly in highly mobile environments. While the structured nature of cell-based networks facilitates efficient resource allocation, interference management, and network organization, it also imposes limitations including the following [28, 33]:

- Inter-Cell Interference:

  Since adjacent cells operate independently, interference from neighboring BSs can degrade performance, especially in dense deployments.

- Coverage Gaps:

  Users at the cell edges often experience weaker signals and lower data rates due to their distance from the serving BS.

- Handover Delays:

  As users move between cells, frequent handovers can lead to latency and connec-

tion instability, particularly in high-mobility scenarios.

To mitigate these challenges, techniques like coordinated beamforming [34, 35], interference management [36], and network densification (deploying more BSs in smaller cells) [37] have been introduced. However, these solutions still rely on the fundamental cellular structure, which inherently limits network performance in ultra-dense and highly dynamic environments.

1.2.2 Transition to Cell-Free MIMO Networks

Cell-free systems represent a significant departure from traditional cellular network architectures by distributing numerous APs or BSs across the coverage area, rather than grouping them into fixed cells. Building on the principles of cell-free systems, cell-free MIMO systems—also known as distributed MIMO systems—represent an innovative evolution of traditional cellular networks [12]. These systems address key challenges faced by conventional cell-based architectures by enabling full cooperation among all distributed BSs across the entire network, as shown in Fig. 1.2. Cell-freee network architecture eliminates the need for rigid cell boundaries, resulting in seamless and uniform coverage [38,39]. In Fig. 1.2, radio links are the wireless connections between user equipment (UEs) and BSs, enabling communication over the air using signals like LTE or 5G. On the other hand, fronthaul links connect BSs to a central processing unit (CPU), typically using fiber-optic cables, Ethernet, or wireless microwave links. While radio links serve end-users, fronthaul links help coordinate and process data between distributed network elements in cell-free MIMO networks. Through coordinated beamforming and distributed signal processing, these systems provide more consistent coverage, mitigate interference, and enhance overall network capacity, even in areas previously challenged by weak signals or congestion [40]. The ability for all BSs to work togethersignificantly improves the quality of service of wireless networks. Moreover, the system's design en-

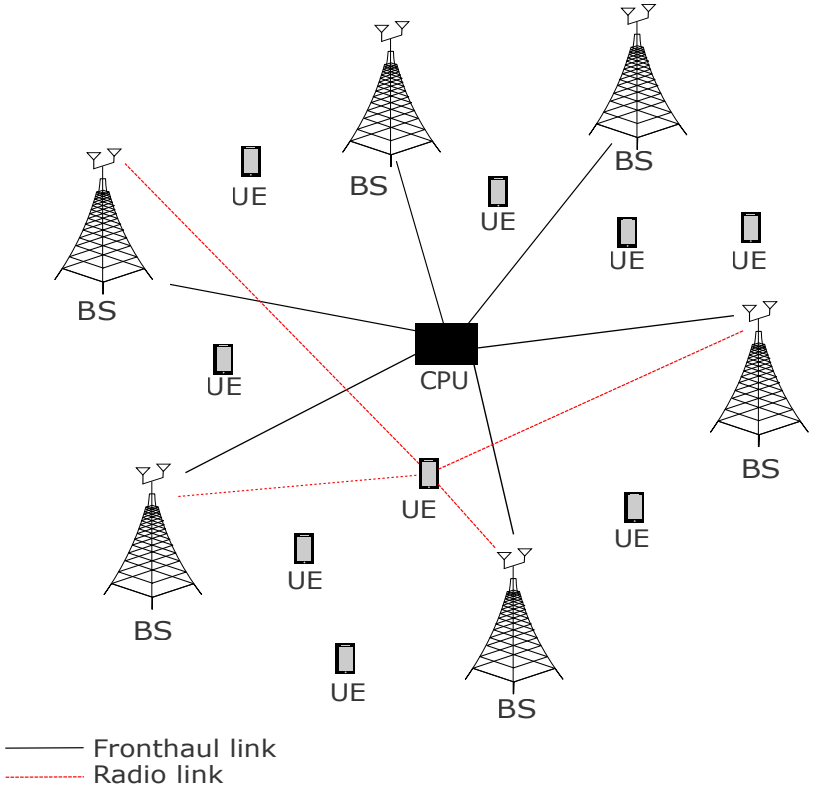

Figure 1.2: Cell-free MIMO network architecture

ables the dynamic allocation of resources—such as power and bandwidth—adapted in real-time based on network conditions and user requirements [41].

Additionally, cell-free MIMO systems offer significant advantages in scalability, flexibility, and robustness. The spatial diversity provided by the large number of BSs ensures users experience a more uniform quality of service across the entire network, minimizing performance degradation due to fading or shadowing [42]. This is especially beneficial in complex environments with fluctuating wireless channel conditions. Moreover, by supporting massive MIMO techniques, where BSs are equipped with a large number of antennas, cell-free MIMO systems can increase system capacity and spectral efficiency, making them well-suited for the future demands of 5G and beyond [13, 14, 43].

Furthermore, cell-free MIMO systems have the potential to overcome energy effi-

ciency challenges faced by traditional cellular networks [31]. By distributing the communication load across many BSs instead of relying on a few high-power BSs, energy consumption can be optimized, leading to more sustainable network operations. The coordinated nature of the system also reduces power requirements for individual BSs, as they are no longer required to transmit at maximum power to reach users located at the cell edges [32].

However, implementing cell-free networks does introduce new challenges that need to be addressed [44–47]:

- High Backhaul Requirements:
  Coordinating a large number of APs necessitates efficient data exchange, putting pressure on the backhaul network.

- Computational Complexity:
  Joint signal processing across multiple APs requires advanced optimization algorithms to ensure efficient operation.

- Scalability Issues:
  Managing a fully distributed network with many users demands efficient user association and resource allocation strategies to maintain optimal performance.

Despite these challenges, the cell-free MIMO approach holds great promise in improving the performance, scalability, and energy efficiency of future wireless networks.

1.2.3 Key Differences Between Cell-Based and Cell-Free MIMO Networks

The fundamental differences between cell-based and cell-free MIMO networks can be summarized as in Table 1.1.

Table 1.1: Comparison of Cell-Based and Cell-Free MIMO Networks

Feature	**Cell-Based Networks**	**Cell-Free MIMO Networks**
User Association	Connects to a single BS within a cell	Dynamically served by multiple APs
Interference Management	High inter-cell interference	Lower interference due to coordination
Handover Process	Frequent handovers between BSs	No handovers, seamless connectivity
Coverage	Uneven, weaker at cell edges	More uniform due to joint transmission
Implementation Complexity	Requires network planning for cells	Higher computational and backhaul demands

1.3 Role of IRS in Enhancing Wireless Communication Networks

IRSs offer a promising solution to address many of the challenges faced by wireless networks, both cell-based and cell-free networks [22, 48]. By controlling the phase, amplitude, and polarization of reflected signals, IRS can dynamically shape the wireless environment to reduce interference, enhance signal strength, and improve coverage [16–18, 49, 50]. This technology can help alleviate spectrum limitations by enabling more efficient spectrum usage and reducing congestion. Additionally, IRS can enhance energy efficiency by optimizing signal paths, reducing power consumption for both transmitters and receivers [19]. Its ability to create favorable signal conditions can also mitigate

the effects of obstacles, mobility, and environmental changes, ensuring more reliable communication [21]. By integrating IRS into network designs, we can achieve smarter, more adaptive, and high-performing wireless systems that overcome many of the current limitations.

1.3.1 What is an IRS and How It Works

IRSs are a revolutionary technology designed to enhance wireless communication by controlling the propagation of electromagnetic (EM) waves. An IRS typically consists of a large array of passive, low-cost, and programmable reflecting elements, often implemented as metasurfaces [51]. These elements can be individually tuned to manipulate the phase, amplitude, and polarization of incoming wireless signals, effectively shaping the wireless environment.

The operation of IRS relies on precise control mechanisms. Each reflecting element within the surface is equipped with tunable components, such as varactor diodes [52] or micro-electro-mechanical systems (MEMS) [53], which allow adjustments to their EM response. By programming the surface to reflect signals in specific directions or with certain properties, IRS can create constructive interference at desired locations and destructive interference elsewhere. This capability enables the optimization of signal quality, coverage, and overall network performance.

1.3.2 Advantages of IRS in Mitigating Wireless Network Challenges

Wireless networks face numerous challenges, including interference, limited spectrum availability, energy inefficiency, and environmental disruptions [54, 55]. IRS can play a pivotal role in addressing these issues:

- Reducing Interference and Noise

  By directing signals along optimal paths and suppressing unwanted ones, IRS can create a more controlled propagation environment. This targeted reflection minimizes the overlap of signals from multiple devices and enhances the signal-to-interference-plus-noise ratio (SINR), leading to improved network reliability and data quality.

- Enhancing Spectrum Efficiency

  The wireless spectrum is a finite resource, and its efficient utilization is critical to meeting the growing demand for data transmission. IRS enables more effective spectrum use by shaping beams and avoiding unnecessary signal spillovers. This precise control allows for better frequency reuse, reducing congestion and increasing the capacity of wireless systems.

- Boosting Coverage and Reliability

  In urban environments and smart cities, where buildings and other obstacles often degrade signal quality, IRS can act as virtual relay stations. By redirecting signals around physical barriers, IRS ensures better coverage and uninterrupted connectivity. This capability is particularly beneficial in dense urban areas or locations with challenging propagation conditions.

- Adapting to Environmental Changes

  The wireless environment is dynamic, with factors like mobility, obstacles, and weather affecting signal propagation. IRS can dynamically reconfigure its reflective properties to adapt to these changes in real-time. By continuously optimizing signal paths, it ensures stable and reliable communication even in rapidly changing or unpredictable scenarios.

1.3.3 Drawbacks and Limitations of IRS

Despite its numerous advantages, IRS is not without challenges. Some of the key drawbacks include [49, 56–59]:

- High Control Overhead

  To achieve optimal performance, IRS requires precise and continuous coordination between its reflective surface, BSs, and user devices. The computational demands of this coordination are significant, primarily due to the large number of reflective elements required for enhanced communication. In most cases described in the literature, each IRS element is controlled individually, meaning that every element needs a separate control signal to adjust its behavior. This independent control mechanism leads to the simultaneous management of a vast number of control signals, significantly increasing the overall control overhead. Such a requirement makes the implementation and operation of IRS in large-scale systems a challenging task.

- Wiring Complexities and Energy Losses

  While IRS operates passively in terms of signal reflection, it still requires power for tuning and control mechanisms. Distributing power and managing wiring for thousands of reflective elements can introduce energy losses and increase the overall complexity of the system. This wiring challenge can offset some of the energy efficiency benefits that IRS aims to provide.

- Slow Reconfiguration Times

  The technologies used in IRS, such as MEMS or varactor diodes, and the high control overhead often limit the speed of reconfiguration. For optimal performance, IRS typically requires individual control of a large number of reflective elements, each demanding its own control signal. This need for extensive and simultane-

ous signal management further slows down the system's ability to switch between configurations.

1.4 Motivation

The challenges highlighted previously underscore the need for innovative approaches to overcome the limitations of existing IRS implementations. In the current literature, phase shifts of IRS elements are predominantly controlled on an element-wise basis, requiring each element to be individually configured. While effective in theory, this method introduces significant control overhead and operational complexity, particularly for large-scale IRS systems with numerous elements.

Motivated by these challenges, this thesis proposes a novel Kronecker-based approach to streamline the control and operation of IRS. By addressing the inefficiencies of element-wise control and developing a more cohesive and scalable approach, this work aims to reduce control overhead, enhance reconfiguration speed, and improve overall system performance. Furthermore, the proposed method is evaluated in both cell-based and cell-free network models to demonstrate its versatility and effectiveness in different network architectures.

1.5 Contributions

The first part of this thesis introduces a new Kronecker-based method for controlling the phase shifts of IRS elements. This method is designed to reduce the control overhead and improve the overall throughput of the communication network, referred to as the good-put. By utilizing the Kronecker structure, the proposed approach simplifies the process of adjusting the phase shifts by hugely reducing the required number of control signals, making it both scalable and efficient, particularly for systems with a large

number of IRS elements.

To test the proposed method, a simple downlink communication model is used. An optimization problem is formulated based on the MMSE criterion, which involves jointly optimizing the phase shifts of the IRS and the beamforming matrix at the BS. Since the optimization problem is multi-variable and non-convex, an AO technique is applied to find near-optimal solutions effectively.

The system's performance is evaluated using two key metrics: the sum-rate, which measures the total capacity of the network, and the good-put, which reflects the actual data throughput. Under the assumption of perfect channel state information (CSI), numerical results are obtained to evaluate the performance of the proposed phase shift control method.

Simulations are conducted to study how the number of IRS elements and the BS transmit power affect system performance and the results clearly show that the proposed Kronecker-based control method performs better than traditional element-wise control methods, achieving higher throughput and more efficient control.

Building on these findings, the Kronecker-based control method is extended to a more complex cell-free MIMO system with multiple IRSs, addressing both uplink and downlink communication scenarios. For each scenario, an optimization problem is formulated based on the MMSE criterion, considering the added complexity of having distributed BSs and multiple IRSs.

The optimization problems for the uplink and downlink scenarios are multi-variable and non-convex, and an AO-based approach is used to find optimal solutions. For the uplink, the optimization focuses on jointly adjusting the IRS phase shifts and the receiver matrix at the distributed BSs. For the downlink, the optimization involves jointly designing the beamforming at the BSs, the IRS phase shift matrices, and a scaling factor related to the receivers.

The performance of this cell-free MIMO system is evaluated using sum-rate and

good-put as metrics for both uplink and downlink scenarios. Furthermore, the system performance is analyzed by varying the number of IRS elements, the BS transmit power, and the number of users in the network.

Simulation results reveal that the Kronecker-based phase shift control method enhances good-put performance while ensuring scalability, making it a highly efficient and practical solution for seamless integration into modern wireless communication networks.

1.6 Scholastic Outputs and Achievements

This thesis includes materials previously published, accepted, and submitted in peer-reviewed journals and conferences, as outlined in the table 1.2.

Table 1.2: Summary of publications

Publications	**Appearance**
1. **I. Nimnadini**, A. Mezghani, and E. Hossain, "Low-overhead kronecker-based intelligent reflective surfaces for 5G and beyond," in *IEEE World Forum on Internet of Things (WF-IoT), November 2024.* doi: 10.1109/WF-IoT62078.2024.10811391.	Chapter 2
2. **I. Nimnadini**, A. Mezghani, E.Hossain, "Cell-Free MIMO Systems Enhanced With Kronecker-Based Intelligent Reflective Surfaces" in *IEEE Transactions on Wireless Communications.* (Under review)	Chapter 3

1.7 Thesis Organization and Notations

This thesis is organized into several chapters, each addressing a key aspect of the research on optimizing IRSs in wireless communication networks. Chapter 1 provides an introduction to the topic, outlining the motivation, objectives, and scope of the research. Chapter 2 focuses on a single cell downlink transmission system, where the Kronecker-based phase shift model is introduced, and the optimization problem is formulated and solved to reduce control overhead and improve system efficiency. Chapter 3 extends the Kronecker-based model to more complex cell-free MIMO systems, incorporating multiple IRSs for enhanced coverage, interference mitigation, and performance. This chapter also develops optimization frameworks for both uplink and downlink communication and presents a detailed performance analysis using key metrics such as sum-rate and good-put, and validates the proposed methods through numerical simulations. Finally, Chapter 4 concludes the thesis by summarizing the key contributions and suggesting potential avenues for future research.

Notations: Given any matrix $\mathbf{A}$, $\mathbf{A}^T$, $\mathbf{A}^*$ and $\mathbf{A}^H$ denote its transpose, conjugate, and conjugate transpose, respectively, and $\mathrm{Tr}(\mathbf{A})$ denotes the trace of the matrix $\mathbf{A}$. Kronecker product of two vectors or matrices is represented by $\otimes$. $\mathrm{Diag}(\mathbf{a})$ gives a diagonal matrix with the elements of vector $\mathbf{a}$ in its diagonal and $\mathrm{diag}(\mathbf{A})$ returns the vector containing the diagonal elements of the matrix $\mathbf{A}$. $\|.\|_2$ and $\|.\|_{\mathrm{F}}$ stand for the Euclidean and Frobenius norms, respectively, whereas the expectation operator is indicated by $\mathbb{E}\{.\}$. $\mathbf{I}_N$ denotes the identity matrix of size N.

Chapter 2

Low-Overhead Kronecker-Based Phase Shift Control in Intelligent Reflective Surfaces

2.1 Overview

A novel approach to managing IRS elements is introduced in this chapter, with the goal of significantly reducing the control overhead and complexity inherent in conventional element-wise control methods. Conventional IRS configurations which require separate control signals for each IRS element, are often constrained by intricate design requirements, extensive wiring, complex implementation, high energy consumption, and limited adaptability to dynamic wireless environments. Recent studies have highlighted the potential of IRS to enhance wireless communication performance; however, the complexity associated with controlling individual elements remains a critical challenge, particularly in large-scale deployments. To address these issues, a simplified control mechanism based on a Kronecker-based phase shift model is proposed, enabling structured control

of multiple elements, where control signals are applied row-wise and column-wise. The effectiveness of the proposed method is evaluated using a simple downlink system model, demonstrating its capability to reduce control overhead while maintaining or enhancing key performance metrics such as signal strength, coverage, and energy efficiency. By addressing the practical limitations of conventional approaches, this work provides a foundation for more scalable, cost-effective, and adaptive IRS implementations in future wireless networks.

2.2 Kronecker-based Phase Shift Control Method

The Kronecker-based approach for controlling the phase shifts of the IRS elements is inspired by the inherent Kronecker structure of the array response in planar antenna arrays. In a uniform planar array (UPA) of $M \times N$ elements, the array response can be expressed as the Kronecker product of the steering vectors along the horizontal and vertical dimensions, as in equation (2.1) [60].

$$\mathbf{a}(\varphi, \psi) = \mathbf{a}_x(\varphi, \psi) \otimes \mathbf{a}_y(\varphi, \psi), \tag{2.1}$$

where, $\mathbf{a}_x(\varphi, \psi)$ and $\mathbf{a}_y(\varphi, \psi)$ represent the steering vectors in the x- and y-directions, respectively. Here, φ denotes the elevation angle while ψ denotes the azimuth angle. Since IRS elements passively reflect incident signals with controllable phase shifts, the entire IRS can be modeled as a planar array of reflective elements, analogous to a planar antenna array. Consequently, the array response of an IRS also follows the Kronecker structure too. Motivated by this observation, the Kronecker structure is leveraged to control the phase shifts of the reflected signals more efficiently.

Consider an IRS with $M = M_x \times M_y$ number of reflective elements with M_x and M_y denoting the number of rows and columns, respectively. The phase shift matrix of the

IRS, represented by the diagonal matrix $\mathbf{\Theta} \in \mathbb{C}^{M \times M}$, is defined as a Kronecker product:

$$\mathbf{\Theta} = \mathbf{\Theta}_x \otimes \mathbf{\Theta}_y, \tag{2.2}$$

where, $\mathbf{\Theta}_x \in \mathbb{C}^{M_x \times M_x}$ and $\mathbf{\Theta}_y \in \mathbb{C}^{M_y \times M_y}$ are complex diagonal matrices. These matrices are structured such that their diagonal elements control the phase shifts introduced by the rows and columns of the IRS, respectively. In this model, the i^{th} diagonal element of $\mathbf{\Theta}_x$ is associated with the phase shift applied to the entire i^{th} row of the IRS. This phase shift is controlled by a corresponding signal, denoted as $V_{x,i}$ with $i = 1, ..., M_x$.Similarly, the j^{th} diagonal element of $\mathbf{\Theta}_y$ determines the phase shift applied to the j^{th} column of the IRS. The corresponding control signal for this phase shift is $V_{y,j}$, where $j = 1, ..., M_y$ as shown in Fig. 2.1.

As a result, the phase shift introduced at any specific IRS element, located at the intersection of the i^{th} row and the j^{th} column, is the product of two factors: the i^{th} diagonal element of $\mathbf{\Theta}_x$ and the j^{th} diagonal element of $\mathbf{\Theta}_y$, allowing the total phase shift matrix to be presented as in (2.2). This Kronecker-based structure allows the control of phase shifts at individual IRS elements through a reduced set of control signals. Instead of requiring one unique signal for each IRS element, only $M_x + M_y$ control signals are needed to manage an IRS comprising $M = M_x \times M_y$ elements.

This Kronecker-based method achieves independent phase shifts at each IRS element while significantly simplifying the control mechanism. By reducing the number of required control signals, the approach addresses practical challenges such as hardware complexity, wiring, and energy consumption, making it suitable for large-scale IRS deployments.

In this work, the IRS is assumed to be passive and lossless. As a result, each diagonal element of the phase shift matrices can be expressed in the form $[\mathbf{\Theta}_z]_{(i,i)} = e^{j\theta_{z,i}}$, ensuring that the IRS introduces no additional signal losses and operates solely through phase adjustments. Here, $\theta_z \in (0, 2\pi]$ and $z \in \{x, y\}$.

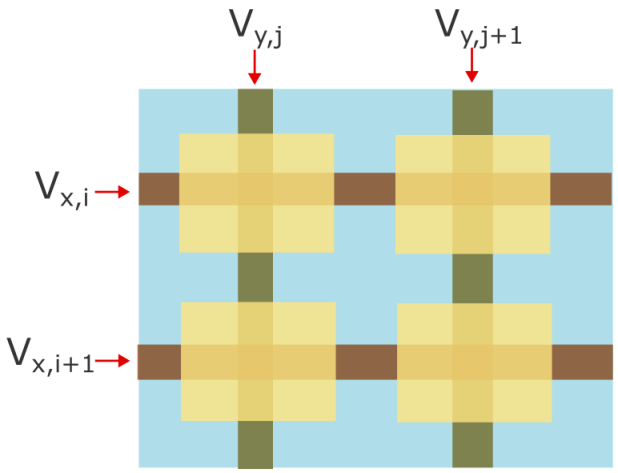

Figure 2.1: Control structure of the IRS

For convenient representation and computation, the following relationships are defined:

$$\mathbf{\Phi}_z = \text{diag}(\mathbf{\Theta}_z), \tag{2.3a}$$

$$\mathbf{\Phi} = \text{diag}(\mathbf{\Theta}), \tag{2.3b}$$

for $z \in \{x, y\}$.

2.3 System, Channel and Signal Models

2.3.1 System Model

The downlink transmission of an IRS-assisted wireless communication system is considered, as illustrated in Fig. 2.2. The BS is equipped with N transmitting antennas and serves K single-antenna users, denoted by U_k, $k \in \{1, \cdots, K\}$. The IRS comprises $M = M_x \times M_y$ reflective elements, where M_x and M_y represent the number of rows and columns, respectively.

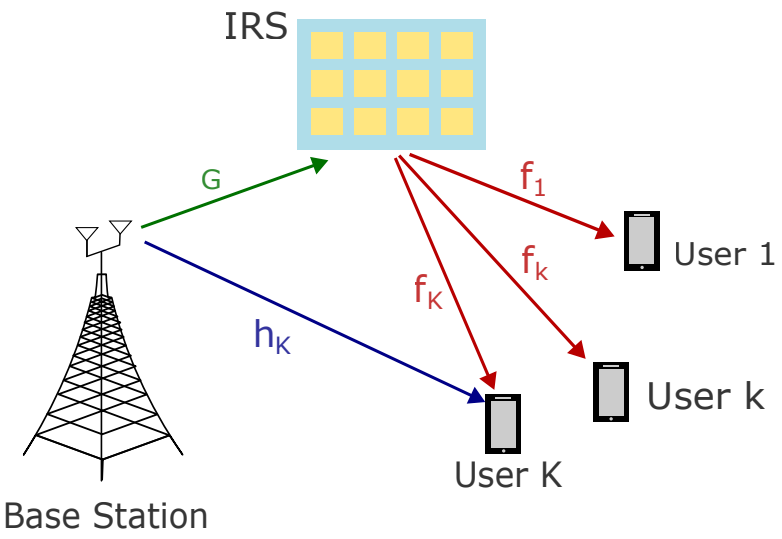

Figure 2.2: Single cell downlink system model

In this system, each downlink user, U_k, receives signals from the BS through two distinct paths: a direct link and a reflected link facilitated by the IRS. The phase shift matrix of the IRS is assumed to follow the Kronecker structure outlined in Section. 2.2.

2.3.2 Channel Model

The channel from the BS to the IRS is denoted by $\mathbf{G} \in \mathbb{C}^{M\times N}$ while $\mathbf{h}_k \in \mathbb{C}^{N\times 1}$ and $\mathbf{f}_k \in \mathbb{C}^{M\times 1}$ denote the channels to the k^{th} user from BS and IRS, respectively. These channels are modelled using the parametric channel model [61], [62] as,

$$\mathbf{G} = \sqrt{L(d_{IRS-BS})} \sum_{q=1}^{Q_{BS-IRS}} c_q \mathbf{a}_{IRS}(\varphi_q, \psi_q)\mathbf{a}_{BS}(\phi_q)^T, \tag{2.4}$$

$$\mathbf{h}_k = \sqrt{L(d_{BS-U_k})} \sum_{q=1}^{Q_{BS-U}} c_{k,q} \mathbf{a}_{BS}(\phi_{k,q})^T, \tag{2.5}$$

$$\mathbf{f}_k = \sqrt{L(d_{IRS-U_k})} \sum_{q=1}^{Q_{IRS-U}} c_{k,q} \mathbf{a}_{IRS}(\varphi_{k,q}, \psi_{k,q}). \tag{2.6}$$

In above equations, d_{IRS-BS}, d_{BS-U_k} and d_{IRS-U_k} represent the distance between IRS and BS, BS and k^{th} user and IRS and k^{th} user, respectively, while $L(d)$ gives the distance-dependent path-loss factor calculated as in (2.7):

$$L(d) = C_0(d_0/d)^{\eta}, \tag{2.7}$$

where d_0 is the reference distance and η is the path-loss exponent. C_0 denotes the path-loss at the reference distance. In (2.4)-(2.6), Q denotes the number of channel paths between the considered elements of the communication system and c denotes channel path gain. Furthermore, $\mathbf{a}_{BS}$ and $\mathbf{a}_{IRS}$ represent the array responses of the BS and the IRS, respectively. These array responses are defined in (2.8) and (2.9) below:

$$\mathbf{a}_{BS}(\phi) = [1, e^{2\pi j \frac{d_b}{\lambda}\cos(\phi)}, ..., e^{2\pi j \frac{d_b}{\lambda}(N-1)\cos(\phi)}]^T, \tag{2.8}$$

$$\mathbf{a}_{IRS}(\varphi,\psi) = \sqrt{|\cos\varphi|} \begin{bmatrix} 1 \\ e^{2\pi j \frac{d_s}{\lambda}\sin\varphi\sin\psi} \\ \vdots \\ e^{2\pi j \frac{d_s}{\lambda}(M_x-1)\sin\varphi\sin\psi} \end{bmatrix} \otimes \begin{bmatrix} 1 \\ e^{2\pi j \frac{d_s}{\lambda}\sin\varphi\cos\psi} \\ \vdots \\ e^{2\pi j \frac{d_s}{\lambda}(M_y-1)\sin\varphi\cos\psi} \end{bmatrix}. \tag{2.9}$$

In (2.8) and (2.9), φ, ψ and ϕ represent the elevation angle, azimuth angle, and angle of departure, respectively. The parameter d_b denotes the spacing between two adjacent antennas at the BS while d_s indicates the spacing between two consecutive elements of the IRS. λ represents the signal wavelength. Moreover, this research is conducted under the assumption of perfect CSI.

2.3.3 Signal Model

BS transmits signals to the downlink users and the vector containing each signal received by the users can be written as follows.

$$\mathbf{y} = \alpha\left(\mathbf{F}^H \text{Diag}(\mathbf{\Phi}_x \otimes \mathbf{\Phi}_y)\mathbf{G}\mathbf{W}\mathbf{s} + \mathbf{H}^H\mathbf{W}\mathbf{s} + \mathbf{n}\right). \tag{2.10}$$

Here, $\alpha \in \mathbb{R}$ is a receiver-related scaling factor, which is assumed to be common for all the users. Moreover, k^{th} columns of $\mathbf{F}$ and $\mathbf{H}$ are $\mathbf{f}_k$ and $\mathbf{h}_k$, respectively. In addition, $\mathbf{W} = [\mathbf{w}_1, \mathbf{w}_2, ..., \mathbf{w}_K] \in \mathbb{C}^{N \times K}$ and $\mathbf{s} = [s_1, s_2, ..., s_K]^T$ denote the beamforming matrix and the transmit signal vector of the BS. In (2.10), the first term denotes the signals received by the reflections through the IRS and the second term denotes the direct signal from the BS, while $\mathbf{n} \sim \mathcal{CN}(0, \sigma^2)$ denotes the additive white Gaussian noise (AWGN).

2.4 Problem Formulation

A problem of minimizing the received symbol error of the downlink users under the MMSE criterion is considered. The total mean squared error (MSE) can be written as follows.

$$\text{MSE} = \sum_{k=1}^{K} \mathbb{E}_{y_k, s_k}\{|y_k - s_k|^2\} = \mathbb{E}_{\mathbf{y},\mathbf{s}}\{||\mathbf{y} - \mathbf{s}||_2^2\}. \tag{2.11}$$

The above expression can be simplified into the following expression.

$$\text{MSE} = ||\alpha \mathbf{H}_t^H \mathbf{W} - \mathbf{I}_K||_F^2 + K\alpha^2\sigma^2, \tag{2.12}$$

where,

$$\mathbf{H}_t^H = \mathbf{F}^H \text{Diag}(\mathbf{\Phi}_x \otimes \mathbf{\Phi}_y)\mathbf{G} + \mathbf{H}^H. \tag{2.13}$$

Finally, the optimization problem that is to be solved is formulated as follows.

$$\text{P1} : \underset{\alpha, \mathbf{F}, \mathbf{\Phi}_x, \mathbf{\Phi}_y}{\arg\min} \quad MSE \tag{2.14a}$$

subject to

$$\text{C1} : ||\mathbf{W}||_F^2 \leq P, \tag{2.14b}$$

$$\text{C2} : |[\mathbf{\Phi}_x]_{(i)}| = 1, \ i = 1, 2, ..., M_x, \tag{2.14c}$$

$$\text{C3} : |[\mathbf{\Phi}_y]_{(j)}| = 1, \ j = 1, 2, ..., M_y. \tag{2.14d}$$

Here, the first constraint represents the transmit power limitations of the BS, with P being the maximum it can achieve and C2 and C3 denote the magnitude constraints of the phase shift vectors.

It is observed that P1 is a non-convex problem with multiple optimization variables. Hence, an AO based algorithm is proposed to solve the above problem.

2.5 Solution Approach

As P1 presents a multi-variable non-convex constrained problem, we propose an AO-based algorithm to obtain the solution by decomposing the problem into two sub-problems as in P11 and P12 below.

$$\text{P11}: \arg\min_{\alpha,\mathbf{W}} \; MSE \tag{2.15a}$$

subject to

$$\text{C1}: ||\mathbf{W}||_F^2 \leq P. \tag{2.15b}$$

$$\text{P12}: \arg\min_{\mathbf{\Phi}_x,\mathbf{\Phi}_y} \; ||\alpha \mathbf{H}_t^H \mathbf{W} - \mathbf{I}_K||_F^2 \tag{2.16a}$$

subject to

$$\text{C2}: |[\mathbf{\Phi}_x]_{(i)}| = 1, \; i = 1, 2, ..., M_x, \tag{2.16b}$$

$$\text{C3}: |[\mathbf{\Phi}_y]_{(j)}| = 1, \; j = 1, 2, ..., M_y. \tag{2.16c}$$

The rest of this section discusses the approaches followed to solve the above two sub-problems.

2.5.1 Beamforming Matrix and Receiver Scaling Factor Optimization

Solving the problem P11 gives the optimal beamforming matrix, $\mathbf{W}^{\text{opt}}$ and the optimal receiver scaling factor, α^{opt}. The problem is a convex problem with respect to the optimization variables and its Lagrangian can be used to find the optimal solution. Lagrangian function corresponding to the problem P11 can be formulated as follows.

$$\mathcal{L}(\lambda, \alpha, \mathbf{W}) = ||\alpha \mathbf{H}_t^H \mathbf{W} - \mathbf{I}_K||_F^2 + K\alpha^2\sigma^2 + \mu(||\mathbf{W}||_F^2 - P), \tag{2.17}$$

where $\mu \in \mathbb{R}$ is the Lagrange multiplier corresponding to the transmit power constraint. By setting the partial derivatives of (2.17) to zero, optimal solutions are obtained as below [61, 62].

$$\alpha^{\text{opt}} = \sqrt{\frac{1}{P}}\sqrt{\text{Tr}[(\mathbf{H}_t\mathbf{H}_t{}^H + \frac{K\sigma^2\mathbf{I}_N}{P})^{-2}\mathbf{H}_t\mathbf{H}_t{}^H]}. \tag{2.18}$$

$$\mathbf{W}^{\text{opt}} = \frac{\sqrt{P}[\mathbf{H}_t\mathbf{H}_t^H + \frac{K\sigma^2\mathbf{I}_N}{P}]^{-1}\mathbf{H}_t}{\sqrt{\text{Tr}[(\mathbf{H}_t\mathbf{H}_t^H + \frac{K\sigma^2\mathbf{I}_N}{P})^{-2}\mathbf{H}_t\mathbf{H}_t^H]}}$$

$$\mathbf{W}^{\text{opt}} = \alpha^{\text{opt}^{-1}}[\mathbf{H}_t\mathbf{H}_t^H + \frac{K\sigma^2\mathbf{I}_N}{P}]^{-1}\mathbf{H}_t. \tag{2.19}$$

Hereby, closed-form solutions are obtained for the optimal beamforming matrix and the receiver scaling factor.

2.5.2 Optimization of Phase Shift Vectors

Solution to the non-convex problem in P12 gives the optimal phase shift vectors, $\mathbf{\Phi}_x^{\text{opt}}$ and $\mathbf{\Phi}_y^{\text{opt}}$. In order to find the optimal solution, one variable is considered to be fixed with respect to the other and the projected gradient descent method is used repeatedly for both variables, until the objective function in P12 converges. For more compact

representation, we use, $\mathbf{A} = \alpha\mathbf{F}$, $\mathbf{B} = \mathbf{GW}$ and $\mathbf{C} = \alpha\mathbf{H}^H\mathbf{W} - \mathbf{I}_K$, which will give the expression in (2.16a) as,

$$E = ||\mathbf{A}\text{Diag}(\mathbf{\Phi}_x \otimes \mathbf{\Phi}_y)\mathbf{B} + \mathbf{C}||_F^2. \tag{2.20}$$

Notice that the gradient of E with respect to $\mathbf{\Phi}_x$ and $\mathbf{\Phi}_y$ are vectors of size $M_x \times 1$ and $M_y \times 1$, respectively. Each of the elements in these vectors can be found by,

$$[\nabla_{\mathbf{\Phi}_x} E]_{(i)} = 2\text{Tr}\{\mathbf{B}[\mathbf{A}\text{Diag}(\mathbf{\Phi}_x \otimes \mathbf{\Phi}_y)\mathbf{B} + \mathbf{C}]^H\mathbf{A}\text{Diag}(\mathbf{y}_i)\}, \tag{2.21}$$

and,

$$[\nabla_{\mathbf{\Phi}_y} E]_{(i)} = 2\text{Tr}\{\mathbf{B}[\mathbf{A}\text{Diag}(\mathbf{\Phi}_x \otimes \mathbf{\Phi}_y)\mathbf{B} + \mathbf{C}]^H\mathbf{A}\text{Diag}(\mathbf{x}_i)\}. \tag{2.22}$$

In (2.21) and in (2.22),

$$\mathbf{y}_i = [\mathbf{0}_{M_y(i-1)}, \mathbf{\Phi}_y, \mathbf{0}_{M_y(M_x-i)}]^T, \tag{2.23}$$

and,

$$\mathbf{x}_i = [\mathbf{0}_{M_x-1}, [\mathbf{\Phi}_x]_{(1)}, \mathbf{0}_{M_y}, ..., [\mathbf{\Phi}_x]_{(M_x)}, \mathbf{0}_{M_y-i}]^T, \tag{2.24}$$

where, $\mathbf{0}_j$ is a vector with j number of zeros. The projection function used is as follows:

$$\mathbf{\Phi}_z^i = \frac{\mathbf{\Phi}_z^i}{|\mathbf{\Phi}_z^i|}. \tag{2.25}$$

Here $\mathbf{\Phi}_z^i$ denotes $\mathbf{\Phi}_z, (z \in \{x, y\})$ at the i^{th} iteration of the projected gradient descent algorithm. The complete steps followed in solving the problem P1 are presented by the **Algorithm 1**.

2.6 Simulation Results

2.6.1 Simulation Parameters

In this section, Monte-Carlo simulation results are presented to validate the proposed method numerically. Simulations were conducted using a 12 × 12 IRS and a BS

Algorithm 1 Joint Optimization of reciever scaling factor, Phase Shift vectors and Beamforming Matrix

Initialize: initial iteration number $i = 0$, initial $\{\mathbf{\Phi}_x^0, \mathbf{\Phi}_y^0\}$, step size μ, accuracy level ϵ and maximum iteration number $N_{\max}$.

Generate the channels, $\mathbf{F}$, $\mathbf{H}$ and $\mathbf{G}$.

repeat

Set the iteration number $i \leftarrow i + 1$.

Compute α using (2.18) and update $\alpha^i = \alpha$.

Compute $\mathbf{W}$ using (2.19) and update $\mathbf{W}^i = \mathbf{W}$.

Compute $\nabla_{\mathbf{\Phi}_x} E$ using (2.21) and update $\mathbf{\Phi}_x^i = \mathbf{\Phi}_x^{i-1} - \mu(\nabla_{\mathbf{\Phi}_x} E)^*$.

Compute $\nabla_{\mathbf{\Phi}_y} E$ using (2.22) and update $\mathbf{\Phi}_y^i = \mathbf{\Phi}_y^{i-1} - \mu(\nabla_{\mathbf{\Phi}_y} E)^*$.

Project each element of $\mathbf{\Phi}_x^i$ and $\mathbf{\Phi}_y^i$ as in (2.25)

Compute the objective based on the newly obtained values.

until Objective converges below the desired accuracy level ϵ or number of iterations exceeds $N_{\max}$.

return $\alpha, \mathbf{W}, \mathbf{\Phi}_x$ and $\mathbf{\Phi}_y$.

equipped with 12 transmitting antennas and results were obtained for two scenarios: one with a single downlink user and the other with four downlink users. For the simulations, the distances from the BS to the IRS and from the BS to the downlink users were each assumed to be 500 meters. Meanwhile, the distances between the IRS and the users were uniformly distributed within the range of 10 meters to 50 meters. The number of channel paths was set to $Q_{BS-S} = 8$, $Q_{BS-U} = 2$ and $Q_{S-U} = 2$. Channel path gains of all three channels were assumed to be in a complex normal distribution with zero mean and unit variance. The path loss exponents were set to 2.5 for both the BS-to-IRS and BS-to-user channels and 3.7 for the IRS-to-user channels. The variance of AWGN was considered as, $\sigma^2 = -100$ dBm, and the transmit power of BS was varied from 0 dBm to 50 dBm.

2.6.2 Performance Evaluation

To evaluate the performance of the Kronecker-based IRS control method, two key performance metrics are employed: sum-rate and goodput. These metrics are compared with those achieved by two alternative IRS control methods. The first method, referred to as the Conventional IRS model, controls the phase shift of each IRS element individually. The second method assigns random, unoptimized phase shifts to the IRS elements. Furthermore, the impact of key system parameters, specifically, the effects of the number of IRS elements per surface and the BS's transmit power on overall system performance is analyzed using these metrics.

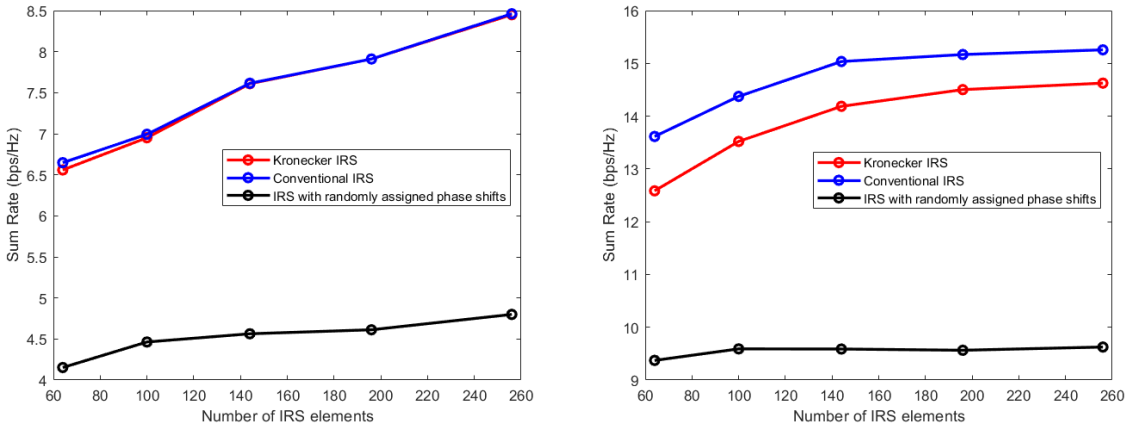

(a) $K = 1$ and $P = 30$ dBm. (b) $K = 4$ and $P = 30$ dBm.

Figure 2.3: Sum-rate variation with number of IRS elements in the presence of (a) one and, (b) four downlink user(s)

Sum-Rate Evaluation

Sum-rate or the total data rate that can be transmitted from the BS to the downlink users of the considered wirelesss communication system is calculated by 2.26.

$$R = \sum_{k=1}^{K} \log_2 \left(1 + \frac{|\mathbf{h}_{t_k}^H \mathbf{w}_k|^2}{\sigma^2 + \sum_{i \neq k} |\mathbf{h}_{t_k}^H \mathbf{w}_i|^2} \right), \tag{2.26}$$

where, $\mathbf{h}_{t_k}^H = \mathbf{f}_k^H \text{Diag}(\mathbf{\Phi}_x \otimes \mathbf{\Phi}_y)\mathbf{G} + \mathbf{h}_k^H$.

The number of IRS elements plays a pivotal role in enhancing the overall sum-rate of the system. With an increasing number of IRS elements, the system gains improved beamforming precision, enabling the IRS to direct the transmitted signals more effectively toward the intended users. This results in a notable enhancement in the SINR, which is essential for boosting the downlink sum-rate. The results presented in Fig. 2.3 validate that a larger IRS significantly enhances signal delivery. Among the models compared, the conventional IRS achieves the highest sum-rate. However, the Kronecker-based IRS model demonstrates nearly equivalent performance when a single downlink user is considered. As the number of users increases, although the Kronecker-

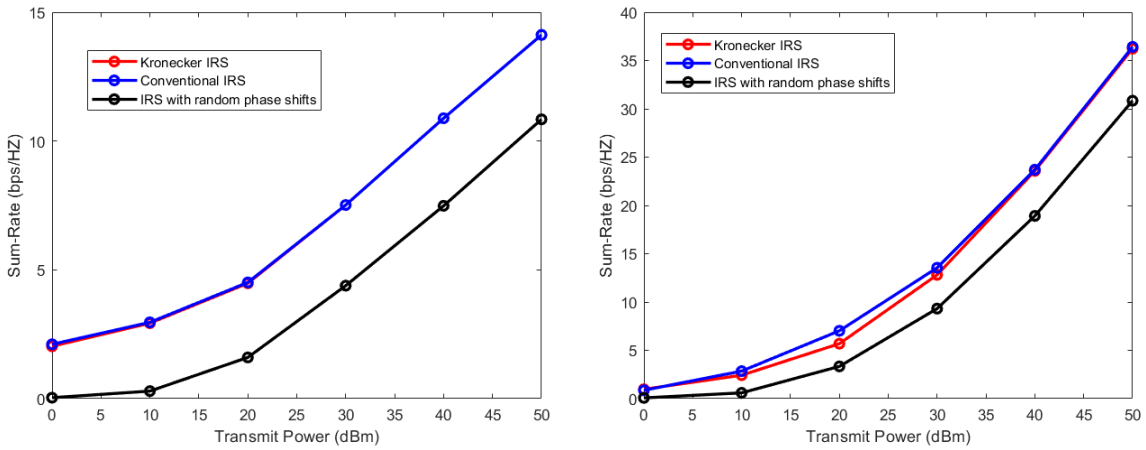

(a) $K = 1$ and $M = 144$.

(b) $K = 4$ and $M = 144$.

Figure 2.4: Sum-rate variation with BS transmit power in the presence of (a) one and, (b) four downlink user(s)

based IRS exhibits slightly lower performance, the difference is minimal, suggesting that it remains a strong alternative. On the contrary, the IRS with random phase shifts exhibits substantially lower performance due to the lack of optimized phase alignment, leading to inefficient signal reflections.

Similarly, the impact of transmit power on the sum-rate is illustrated in Fig. 2.4. As transmit power increases, the downlink sum-rate improves due to stronger received signals at the user end. However, the effectiveness of this improvement heavily depends on the optimization of IRS phase shifts. The model with random phase shifts consistently yields the lowest sum-rate, reaffirming that unoptimized phase control severely limits system performance. Both the conventional and Kronecker-based IRS models demonstrate significant sum-rate improvements with increased transmit power, with the Kronecker-based IRS maintaining a performance level almost overlapping with the conventional IRS. The slight performance difference between the two optimized models suggests that the Kronecker-based IRS remains an efficient alternative.

Good-Put Evaluation

Good-put in a wireless network refers to the effective data rate delivered to the user, accounting for both the useful transmitted information and the overhead associated with network operations, such as control signaling. It adjusts the raw sum-rate by subtracting the resources consumed by system overhead, providing a more realistic measure of the network's efficiency in delivering payload data. For the considered downlink communication model, good-put calculation can be denoted as in (2.27) [63].

$$GP = \left(1 - \frac{bM_{IRS}}{\eta N_s}\right) R, \tag{2.27}$$

where R denotes the sum-rate, representing the total achievable data rate across the network which is calculated using (2.26). The term M_{IRS} corresponds to the number of IRS elements which contribute to overhead due to their control requirements, while b is the number of bits required to configure each IRS element in a single time slot. The spectral efficiency of the communication link is represented by η and N_s is the number of symbols transmitted within the coherence interval. For the simulations, the parameters are set as follows: $b = 2$ bits per IRS element per time slot, $\eta = 2$ bits per second per Hertz (bps/Hz), and $N_s = 1000$ symbols per slot. Note that for the Kronecker-based IRS, the number of IRS elements is given by $M_{IRS} = (M_x + M_y)$, while for a conventional IRS, it is $M_{IRS} = (M_x \times M_y)$. Additionally, for IRS configurations where random phase shifts are assigned, the goodput is equivalent to the sum-rate, as these IRSs do not require any control signaling.

Fig. 2.5(a) and Fig. 2.5(b) illustrate how the good-put performance varies across the three models (Kronecker IRS, conventional IRS, and randomly assigned IRS) as the number of IRS elements increases, for the scenarios with a single downlink user and 4 users, respectively.

From the results, it is evident that the good-put of the conventional IRS model remains relatively stagnant with a single downlink user and reduces gradually with

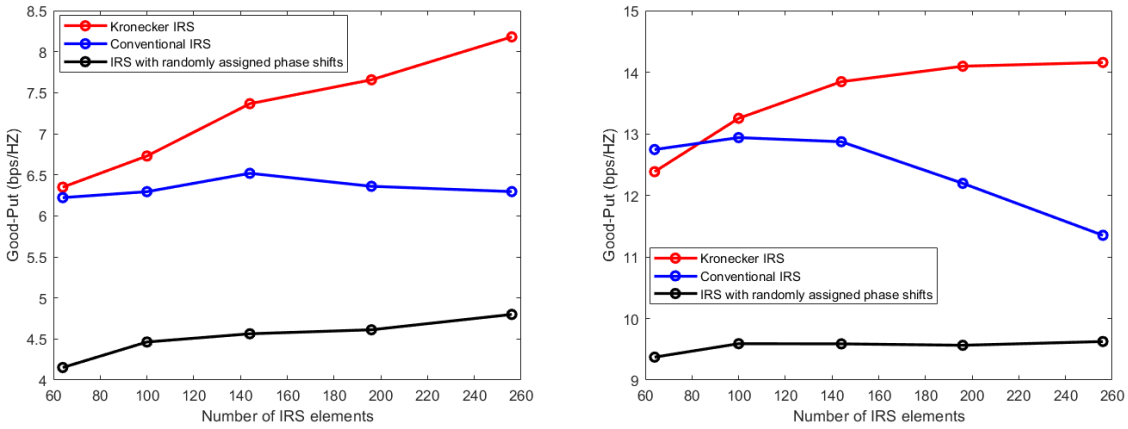

(a) $K = 1$ and $P = 30$ dBm. (b) $K = 4$ and $P = 30$ dBm.

Figure 2.5: Good-put variation with number of IRS elements in the presence of (a) one and, (b) four downlink user(s)

multiple users as the number of IRS elements increases. In contrast, the Kronecker-based IRS model demonstrates a consistent and substantial improvement in good-put performance as the number of elements grows. This trend highlights the scalability advantage of the Kronecker IRS model, which is a critical aspect of IRS design since achieving significant performance gains typically requires a large number of reflecting elements. The gap in good-put performance between the Kronecker IRS and the conventional IRS also widens with an increasing number of elements, further validating the superior efficiency of the proposed Kronecker-based method.

One key observation is that, although the Kronecker IRS model may result in a slight reduction in the sum-rate of the network due to structural restrictions imposed on the phase-shifting matrix, this trade-off is entirely offset by the significant gains achieved in terms of reduced control overhead. The Kronecker model's structured design minimizes the signaling requirements and computational complexity associated with configuring the IRS phase shifts, making it particularly advantageous for large-scale deployments.

In contrast, the conventional IRS model demands a higher number of control signals

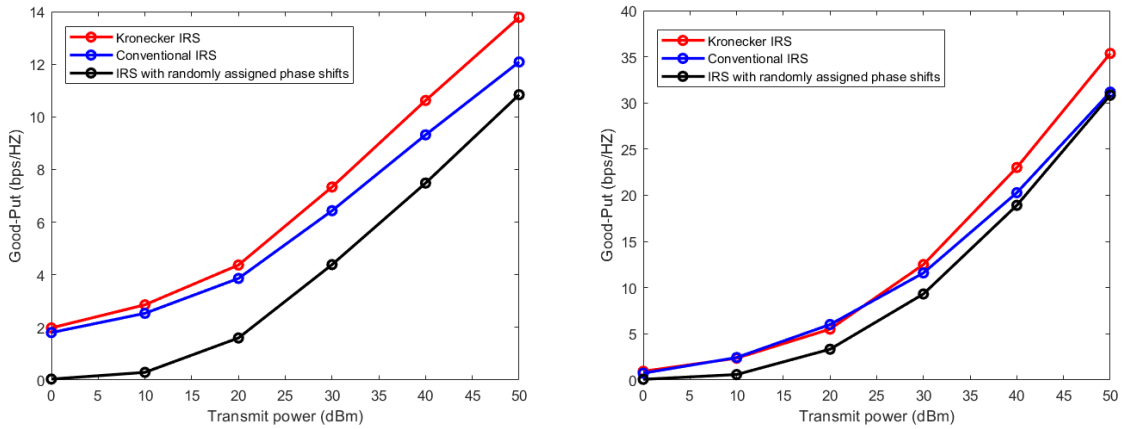

(a) $K = 1$ and $M = 144$.

(b) $K = 4$ and $M = 144$.

Figure 2.6: Good-put variation with BS transmit power in the presence of (a) one and, (b) four downlink user(s)

and involves intricate optimization processes that become increasingly challenging as the IRS scales. This leads to higher power consumption, increased implementation complexity, and diminished practicality for real-world systems. The Kronecker IRS model avoids these pitfalls by exploiting the separable structure of the Kronecker product, which allows for efficient optimization without compromising the scalability or adaptability of the system.

Fig. 2.6(a) and Fig. 2.6(b) extend this analysis by exploring the impact of increasing the BS transmit power on the good-put performance for the three IRS models. The Kronecker IRS model exhibits a rapid and substantial increase in good-put with higher transmit power, significantly outperforming the conventional IRS model in the high signal-to-noise ratio (SNR) regime (transmit power $>$ 30 dBm). While the conventional model shows comparable or slightly better performance in low-SNR scenarios with multiple users, this advantage diminishes as the transmit power increases, where the Kronecker model takes the lead.

Moreover, the IRS with randomly assigned phase shifts demonstrates the poorest

performance among the three models. This outcome aligns with theoretical expectations, as random phase assignments fail to coherently align the reflected signals at the receiver, resulting in destructive interference rather than constructive gains.

The combined results demonstrate that the Kronecker IRS model not only achieves superior good-put performance but also offers significant implementation advantages. Its structured optimization, contrary to being limited, is specifically designed to reduce overhead while ensuring sufficient flexibility to adapt to varying network conditions. This makes it a practical solution for large-scale IRS deployments, where traditional methods struggle due to their high complexity.

In conclusion, while the conventional IRS model has certain advantages in low-SNR networks with minimal transmit power, its limitations in terms of scalability, power consumption, and control signal overhead make it less viable for modern wireless networks. On the other hand, the proposed Kronecker IRS model excels in balancing performance and complexity, making it a more advantageous option for scenarios requiring large-scale IRS and robust good-put performance, particularly in high-SNR regimes.

2.7 Conclusion

In this chapter, a novel method for controlling IRSs in wireless communication networks has been introduced, with the goal of enhancing practical feasibility. To validate the model, a simple downlink transmission network was considered. A non-convex optimization problem was formulated based on the MMSE criterion, and an AO approach was employed to obtain the solution. The Lagrangian method and a projected gradient method were utilized, and the numerical results confirmed that the proposed Kronecker-based method for controlling the IRS is more effective than adjusting the phase shifts of individual IRS elements independently.

Chapter 3

Cell-Free MIMO Systems Enhanced with Kronecker-Based Intelligent Reflective Surfaces

3.1 Overview

Building upon the foundation established in the previous chapter, where the Kronecker-based phase shift model for IRS control was validated in a single cell downlink transmission network, this chapter explores the extension of this model to more complex cell-free MIMO network scenarios. In this extended model, multiple IRSs are incorporated into the system to further enhance signal propagation, improve coverage, and mitigate interference.

A common belief in IRS-assisted wireless networks is that achieving optimal network performance necessitates increasingly complex phase shift control methods, particularly as network complexity grows. It is often assumed that more sophisticated control mechanisms are essential to fully exploit the benefits of IRS elements. However, this chapter

challenges that notion by demonstrating that even with a reduced-complexity control approach, superior performance can still be achieved. This is shown through an analysis of a cell-free MIMO system with multiple base stations, IRSs, and users. By employing a structured Kronecker-based phase shift design, efficient IRS control can be maintained without relying on excessively complicated control mechanisms. The main contributions of this chapter are summarized as follows:

- *Uplink Optimization*: An optimization problem is formulated for uplink communication in a cell-free MIMO system. The problem focuses on the joint optimization of IRS phase shifts and the receiver matrix at the distributed BSs, aiming to enhance uplink performance.

- *Downlink Optimization*:A joint optimization framework is proposed for downlink communication. This framework simultaneously optimizes the beamforming at distributed BSs and the IRS phase shift matrices to improve downlink communication performance.

- *Performance Analysis*: The system's performance is thoroughly analyzed using two key metrics: sum-rate and good-put. These metrics are evaluated for both uplink and downlink communication scenarios to assess the effectiveness of the Kronecker-based control method.

- *Numerical Validation*: Numerical simulations are conducted to validate the proposed methods. The results demonstrate that the Kronecker-based phase shift control method significantly outperforms the traditional element-wise phase shift control approach in terms of both uplink and downlink performance.

3.2 System, Channel and Signal Models

3.2.1 System Model

Both the uplink and the downlink communication in a multi-user cell-free MIMO system with multiple IRSs are considered as shown in Fig. 3.1(a) and Fig. 3.1(b), respectively. The system consists of B number of distributed BSs and R number of IRSs. Each BS is equipped with N number of receiving/ transmitting antennas and each IRS consists of $M = M_x \times M_y$ number of reflective elements with M_x and M_y denoting the number of rows and columns, respectively. These IRSs are assumed to be placed at fixed locations, especially in regions where the direct path between users and BSs may be weak or obstructed. There are K number of single antenna users ($\mathrm{U}_k,\ k \in \{1, \cdots, K\}$). It is assumed that each BS communicates with each downlink user, U_i utilizing the direct link and the reflected links through IRSs.

The Kronecker-based phase shift control method explained in Section 2.2 is adopted here, for all the R IRSs, which results the phase shift vectors of the IRSs to be expressed as in (3.1).

$$\mathbf{\Phi}_r = \mathbf{\Phi}_{x_r} \otimes \mathbf{\Phi}_{y_r}, \tag{3.1}$$

where $\mathbf{\Phi}_{x_r} \in \mathbb{C}^{1\times M_x}$ and $\mathbf{\Phi}_{y_r} \in \mathbb{C}^{1\times M_y}$ are the row-wise and column-wise phase shift vectors corresponding to the r^{th} IRS, respectively. In this approach, the $M = M_x \times M_y$ phase shifts of each IRS are represented using only $M_x + M_y$ control signals. Given that practical IRS deployments typically consist of a large number of elements, this Kronecker-based method provides a significant reduction in the number of required control signals. Moreover, this reduction is particularly beneficial in scenarios involving multiple IRSs, as considered in this study. By minimizing control overhead, this approach offers a highly efficient and scalable solution for managing IRS phase shifts in complex network deployments.

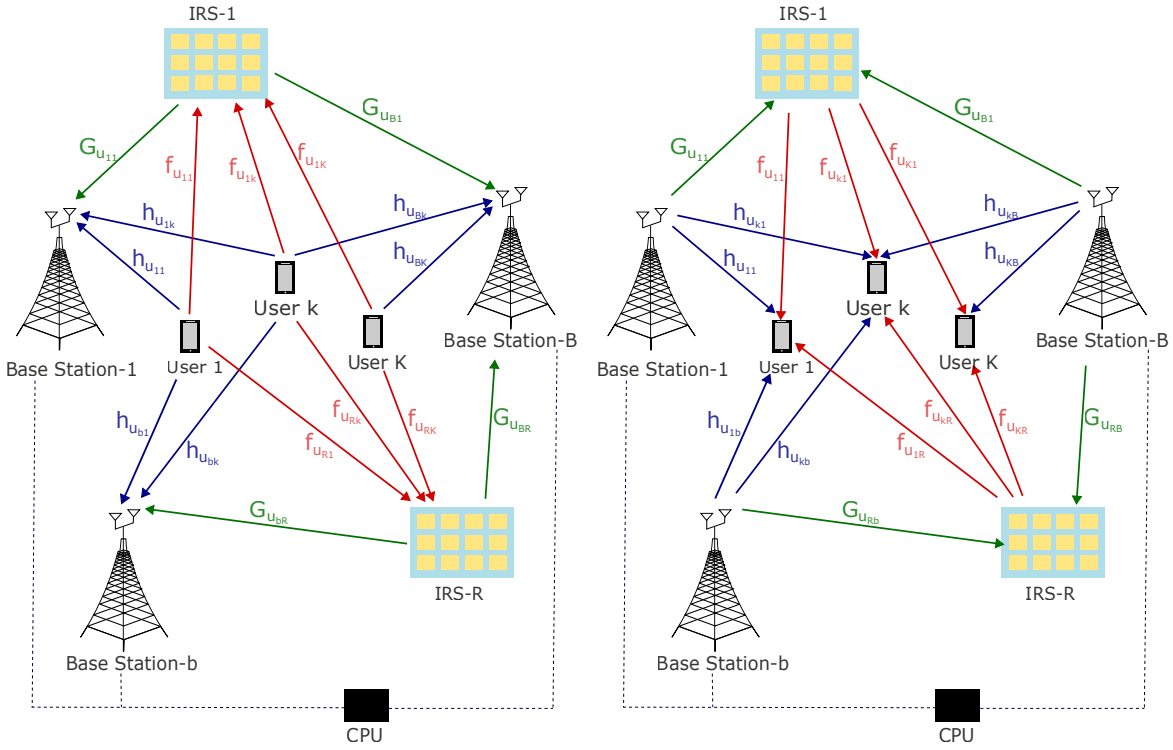

(a) Uplink model.

(b) Downlink model.

Figure 3.1: (a) Uplink and, (b) downlink cell-free system models.

For simplicity, the phase shift vectors of all the Kronecker IRSs are combined into a single vector, as shown in (3.2):

$$\begin{aligned} \mathbf{\Phi} &= [\mathbf{\Phi}_1, ..., \mathbf{\Phi}_R], \\ \mathbf{\Phi} &= [\mathbf{\Phi}_{x_1} \otimes \mathbf{\Phi}_{y_1}, ..., \mathbf{\Phi}_{x_R} \otimes \mathbf{\Phi}_{y_R}]. \end{aligned} \tag{3.2}$$

The phase shift matrices of the IRSs, $\mathbf{\Theta}$ are related with $\mathbf{\Phi}$ as in (3.3):

$$\mathbf{\Theta}_{z_r} = \text{Diag}(\mathbf{\Phi}_{z_r}), \tag{3.3a}$$

$$\mathbf{\Theta}_r = \text{Diag}(\mathbf{\Phi}_r), \tag{3.3b}$$

$$\mathbf{\Theta} = \text{Diag}(\mathbf{\Phi}), \tag{3.3c}$$

for $z \in \{x, y\}$.

In this study, any diagonal element of these matrices can be presented in the format of $[\mathbf{\Theta}_z]_{(i,i)} = e^{j\theta_{z,i}}$ as all IRSs are considered as passive and lossless. Here, $\theta_z \in (0, 2\pi]$ and $z \in \{x, y\}$.

3.2.2 Channel Model

The direct channels between the BSs and the users are denoted by $\mathbf{h}_{ij}$, where i represents the destination and j represents the source. Using the same notation, the channels between the IRSs and the BSs are represented by $\mathbf{G}_{ij}$, while the channels between the IRSs and the users are represented by $\mathbf{f}_{ij}$. These channels are modeled using the parametric channel model [56, 60, 61] as follows.

$$\mathbf{h}_{ij} = \sqrt{L(d_{ij})} \sum_{q=1}^{Q_{ij}} c_q \mathbf{a}_{BS}(\phi_q)^T, \tag{3.4}$$

$$\mathbf{G}_{ij} = \sqrt{L(d_{ij})} \sum_{q=1}^{Q_{ij}} c_q \mathbf{a}_{IRS}(\varphi_q, \psi_q) \mathbf{a}_{BS}(\phi_q)^T, \tag{3.5}$$

$$\mathbf{f}_{ij} = \sqrt{L(d_{ij})} \sum_{q=1}^{Q_{ij}} c_q \mathbf{a}_{IRS}(\varphi_q, \psi_q). \tag{3.6}$$

Parameters in the above equations are described in the Section 2.3.2.

Uplink Communication

In the uplink communication system shown in Fig. 3.1(a), $\mathbf{h}_{u_{bk}} \in \mathbb{C}^{N\times 1}$ denotes the channel from the k^{th} uplink user to the b^{th} BS. While $\mathbf{f}_{u_{rk}} \in \mathbb{C}^{M\times 1}$ denotes the channel from the k^{th} uplink user to r^{th} IRS, $\mathbf{G}_{u_{br}} \in \mathbb{C}^{N\times M}$ denotes the channel from the r^{th} IRS to the b^{th} BS. With multiple BSs and IRSs, the system involves a significant number of channels. To simplify their representation, these channels are reorganized as follows:

$$\mathbf{H}_{u_b} = [\mathbf{h}_{u_{b1}}...\mathbf{h}_{u_{bK}}] \in \mathbb{C}^{N\times K}, \tag{3.7a}$$

$$\mathbf{H}_{u} = [\mathbf{H}_{u_1}, ..., \mathbf{H}_{u_B}]^T \in \mathbb{C}^{NB\times K}, \tag{3.7b}$$

$$\mathbf{F}_{u_r} = [\mathbf{f}_{u_{r1}}...\mathbf{f}_{u_{rK}}] \in \mathbb{C}^{M\times K}, \tag{3.8a}$$

$$\mathbf{F}_{u} = [\mathbf{F}_{u_1}, ..., \mathbf{F}_{u_R}]^T \in \mathbb{C}^{MR\times K}, \tag{3.8b}$$

$$\mathbf{G}_{u_r} = [\mathbf{G}_{u_{1r}}...\mathbf{G}_{u_{Br}}] \in \mathbb{C}^{NB\times M}, \tag{3.9a}$$

$$\mathbf{G}_{u} = [\mathbf{G}_{u_1}, ..., \mathbf{G}_{u_R}] \in \mathbb{C}^{NB\times MR}. \tag{3.9b}$$

The above arrangement simplifies representation and facilitates subsequent calculations.

Downlink Communication

As shown in Fig. 3.1(b), $\mathbf{h}_{d_{kb}} \in \mathbb{C}^{1\times N}$ denotes the channel from the b^{th} BS to the k^{th} downlink user, while $\mathbf{f}_{d_{kr}} \in \mathbb{C}^{1\times M}$ and $\mathbf{G}_{d_{rb}} \in \mathbb{C}^{M\times N}$ denote the channel from r^{th} IRS to k^{th} downlink user and the channel from b^{th} BS to r^{th} IRS, respectively, in the downlink

communication system. Similar to the uplink model, the channel representation is rearranged as follows:

$$\mathbf{H}_{d_k} = [\mathbf{h}_{d_{k1}} ... \mathbf{h}_{d_{kB}}] \in \mathbb{C}^{1 \times NB}, \tag{3.10a}$$

$$\mathbf{H}_{d} = [\mathbf{H}_{d_1}, ..., \mathbf{H}_{d_K}]^T \in \mathbb{C}^{K \times NB}, \tag{3.10b}$$

$$\mathbf{F}_{d_r} = [\mathbf{f}_{d_{1r}} ... \mathbf{f}_{d_{Kr}}]^T \in \mathbb{C}^{K \times M}, \tag{3.11a}$$

$$\mathbf{F}_{d} = [\mathbf{F}_{d_1}, ..., \mathbf{F}_{d_R}] \in \mathbb{C}^{K \times MR}, \tag{3.11b}$$

$$\mathbf{G}_{d_r} = [\mathbf{G}_{d_{r1}} ... \mathbf{G}_{d_{rB}}] \in \mathbb{C}^{M \times NB}, \tag{3.12a}$$

$$\mathbf{G}_{d} = [\mathbf{G}_{d_1}, ..., \mathbf{G}_{d_R}]^T \in \mathbb{C}^{MR \times NB}. \tag{3.12b}$$

Similar to the uplink communication model, the above arrangement helps streamline the representation of the numerous channels involved.

3.2.3 Signal Model

Uplink Communication

In this scenario, the uplink users are considered to transmit signals to all the BSs through both direct paths and reflected paths via all the IRSs. The vector containing each of the signals received by each BS can be represented as in (3.13):

$$\mathbf{y}_u = \mathbf{H}_u \mathbf{s}_u + \mathbf{G}_u \mathbf{\Theta} \mathbf{F}_u \mathbf{s}_u + \mathbf{n}, \tag{3.13}$$

where $\mathbf{s}_u = [s_1, s_2, ..., s_K]^T$ denotes the transmit signal vector. In (3.13), the first term denotes the the direct signal from the users and the second term denotes signals received by the reflections through the IRSs, while $\mathbf{n} \sim \mathcal{CN}(0, \sigma^2)$ denotes the AWGN.

Downlink Communication

In the downlink communication of the cell-free system, it is assumed that all the BSs transmit to all the users through both direct channels and reflected channels via all the IRSs. Hence, the received signal vector at the users can be written as in (3.14):

$$\mathbf{y}_d = \alpha[(\mathbf{H}_d + \mathbf{F}_d\boldsymbol{\Theta}\mathbf{G}_d)\mathbf{W}\mathbf{s}_d + \mathbf{n}], \tag{3.14}$$

where $\alpha \in \mathbb{R}$ is a receiver-related scaling factor, which is assumed to be common for all the users. $\mathbf{W} \in \mathbb{C}^{NB\times K}$ denotes the beamforming matrix of the BSs, $\mathbf{s}_d \sim \mathcal{CN}(s; 0, 1)$ denotes the transmit signal and $\mathbf{n} \sim \mathcal{CN}(0, \sigma^2)$ denotes the AWGN.

3.3 Problem Formulation

In this section, the problems for both uplink and downlink communication systems are formulated separately, considering the MMSE criterion.

3.3.1 Uplink Communication

For the uplink communication of the considered cell-free system, the transmitted signals and the noise vector are assumed as Gaussian. Hence the MMSE estimator becomes a linear estimator [60]. To formulate the problem, the concept of linear-MMSE (LMMSE) estimation that minimizes the MSE of the network is exploited. When $\mathbf{W}_R$ is the corresponding linear receiver matrix, the estimated vector containing the received signals at the BSs ($\hat{\mathbf{s}}$) can be written as in (3.15):

$$\hat{\mathbf{s}} = \mathbf{W}_R\mathbf{y}_u, \tag{3.15}$$

where $\mathbf{y}_u$ is given in (3.13).The MSE is first calculated based on its definition and then simplified, as shown below:

$$\begin{aligned}
\mathrm{MSE}_u &= \sum_{k=1}^{K} \mathbb{E}_{\hat{s}_k, s_k}\{|\hat{s}_k - s_k|^2\}, && \text{(3.16a)}\\
&= \mathbb{E}_{\hat{\mathbf{s}}, \mathbf{s}_u}\{||\hat{\mathbf{s}} - \mathbf{s}_u||_2^2\}, && \text{(3.16b)}\\
&= P||\mathbf{I}_K - \mathbf{W}_R\mathbf{H}_u - \mathbf{W}_R\mathbf{G}_u\mathrm{Diag}(\mathbf{\Phi})\mathbf{F}_u||_F^2 \\
&\quad + \sigma^2||\mathbf{W}_R||_F^2. && \text{(3.16c)}
\end{aligned}$$

In (3.16a), $\hat{s}_k$ and s_k denote the estimated and the transmitted signal by the k^{th} uplink user, respectively. The simplification steps from (3.16b) to (3.16c) are similar to the derivation in [61]. Moreover, it is assumed that each uplink user transmits with an identical power level of P. Based on this assumption, the problem is formulated as follows:

$$\begin{aligned}
\mathrm{P2}: &\underset{\mathbf{W}_R, \mathbf{\Phi}_{x_r}, \mathbf{\Phi}_{y_r}}{\arg\min} \quad \mathrm{MSE}_u && \text{(3.17a)}\\
&\text{subject to} \\
&\mathrm{C1}: |[\mathbf{\Phi}_{x_r}]_{(i)}| = 1,\ i = 1, 2, ..., M_x, && \text{(3.17b)}\\
&\mathrm{C2}: |[\mathbf{\Phi}_{y_r}]_{(j)}| = 1,\ j = 1, 2, ..., M_y, && \text{(3.17c)}
\end{aligned}$$

where $i = 1, ..., M_x$ for $z = x$ and $i = 1, ..., M_y$ for $z = y$ with $r = 1, ..., R$. The constraints account for the assumption that the considered Kronecker IRSs are passive and lossless.

3.3.2 Downlink Communication

The MMSE criterion is adopted again to analyze the downlink communication in the considered cell-free system:

$$\begin{aligned}
\text{MSE}_d &= \sum_{k=1}^{K} \mathbb{E}_{y_{d_k}, s_{d_k}} \{|y_{d_k} - s_{d_k}|^2\}, && \text{(3.18a)} \\
&= \mathbb{E}_{\mathbf{y}_d, \mathbf{s}_d} \{||\mathbf{y}_d - \mathbf{s}_d||_2^2\}, && \text{(3.18b)} \\
&= ||\alpha[\mathbf{H}_d + \mathbf{F}_d \text{Diag}(\mathbf{\Phi})\mathbf{G}_d]\mathbf{W} - \mathbf{I}_K||_F^2 \\
&\quad + \sigma^2 \text{trace}(\alpha^2). && \text{(3.18c)}
\end{aligned}$$

The complete problem for the downlink communication is formulated as follows.

$$\begin{aligned}
\text{P3}: &\underset{\alpha, \mathbf{W}, \mathbf{\Phi}_{x_r}, \mathbf{\Phi}_{y_r}}{\arg\min} \quad \text{MSE}_d && \text{(3.19a)} \\
&\text{subject to} \\
&\text{C1}: ||\mathbf{W}||_F^2 \leq P_t, && \text{(3.19b)} \\
&\text{C2}: |[\mathbf{\Phi}_{x_r}]_{(i)}| = 1, \ i = 1, 2, ..., M_x, && \text{(3.19c)} \\
&\text{C3}: |[\mathbf{\Phi}_{y_r}]_{(j)}| = 1, \ j = 1, 2, ..., M_y. && \text{(3.19d)}
\end{aligned}$$

Here, the first constraint denoted by C1 denotes the transmit power constraint of the BSs while the constraints C2 and C3 accounts for the passive and losslessness of the Kronecker IRSs.

3.4 Solution Approach

This section presents the solutions to the problems formulated in the previous section.

3.4.1 Uplink Communication

The problem in P2 is a multi-variable constrained optimization problem, which is challenging to solve directly. Therefore, an AO approach is employed to find the solutions by considering two sub-problems as follows:

$$\text{P21}: \arg\min_{\mathbf{W}_R} \; P||\mathbf{I}_K - \mathbf{W}_R\mathbf{H}_u - \mathbf{W}_R\mathbf{G}_u\text{Diag}(\mathbf{\Phi})\mathbf{F}_u||_F^2 + \sigma^2||\mathbf{W}_R||_F^2. \tag{3.20a}$$

$$\text{P22}: \arg\min_{\mathbf{\Phi}_{x_r},\mathbf{\Phi}_{y_r}} \; P||\mathbf{I}_K - \mathbf{W}_R\mathbf{H}_u - \mathbf{W}_R\mathbf{G}_u\text{Diag}(\mathbf{\Phi})\mathbf{F}_u||_F^2 \tag{3.21a}$$

subject to

$$\text{C1}: |[\mathbf{\Phi}_{x_r}]_{(i)}| = 1, \; i = 1, 2, ..., M_x, \tag{3.21b}$$

$$\text{C2}: |[\mathbf{\Phi}_{y_r}]_{(j)}| = 1, \; j = 1, 2, ..., M_y. \tag{3.21c}$$

These two optimization problems are solved independently by fixing all variables except the one being considered, in order to determine the optimal linear receiver matrix and the phase shift vectors of the IRSs. This process is continued iteratively until the results converge and the final optimal solutions are obtained.

Linear Receiver Matrix ($\mathbf{W}_R$) Optimization

The optimum linear receiver matrix, $\mathbf{W}_R^{\text{opt}}$ can be found by solving the unconstrained problem stated in P21. Since the problem is convex and unconstrained, an optimal point must exist [64], and at this optimal point the first derivative of the function is zero, as per the first-order necessary condition. Therefore, the gradient is set to zero to determine the optimum, as shown below:

$$-2P(\mathbf{I}_K - \mathbf{W}_R\mathbf{H}_t)\mathbf{H}_t^H + 2\sigma^2\mathbf{W}_R = 0, \tag{3.22}$$

where,

$$\mathbf{H}_t = \mathbf{H}_u + \mathbf{G}_u \text{Diag}(\mathbf{\Phi})\mathbf{F}_u. \tag{3.23}$$

By simplifying (3.22), the optimal linear receiver matrix, $\mathbf{W}_R^{\text{opt}}$ can be found as in (3.24):

$$\mathbf{W}_R^{\text{opt}} = \mathbf{H}_t^H \left(\mathbf{H}_t \mathbf{H}_t^H + \frac{\sigma^2 \mathbf{I}_{NB}}{P} \right)^{-1}. \tag{3.24}$$

Here, $\mathbf{I}_{NB}$ is an identity matrix of size $NB \times NB$.

Phase Shift Vectors ($\mathbf{\Phi}_{x_r}$ and $\mathbf{\Phi}_{y_r}$) Optimization

Solution to the subproblem P22 gives the optimal phase shift vectors of the IRSs in the cell-free network. Recall that the phase shifts introduced to the rows and columns of each Kronecker IRS are independent of each other. Therefore, the phase-shift vectors for each IRS are optimized separately. To facilitate this, the objective function of the subproblem is reformulated as follows:

$$E_u = P \left\| \mathbf{I}_K - \mathbf{W}_R \mathbf{H}_u - \mathbf{W}_R \sum_{r=1}^{R} \mathbf{G}_{u_r} \text{Diag}(\mathbf{\Phi}_{x_r} \otimes \mathbf{\Phi}_{y_r}) \mathbf{F}_{u_r} \right\|_F^2. \tag{3.25}$$

Notice that (3.25) is convex with respect to $\mathbf{\Phi}_{x_r}$ when $\mathbf{\Phi}_{y_r}$ is fixed and vice versa. Therefore, The projected gradient descent method is used to find the optimum values for the phase-shift vectors. The gradient is calculated as in (3.26) and (3.27) to find the minimum of E_u:

$$\frac{\partial E_u}{\partial [\mathbf{\Phi}_{x_r}]_i} = -2P \text{Tr} \left\{ \left[\text{Re} \left(\mathbf{G}_{u_r}^H \mathbf{W}_R^H \bar{\mathbf{E}}_{\mathbf{u}} \mathbf{F}_{u_r} \right) \right]^T (\mathbf{T}_{x_i} \otimes \mathbf{\Theta}_{y_r}) \right\}, \tag{3.26}$$

$$\frac{\partial E_u}{\partial [\mathbf{\Phi}_{y_r}]_j} = -2P \text{Tr} \left\{ \left[\text{Re} \left(\mathbf{G}_{u_r}^H \mathbf{W}_R^H \bar{\mathbf{E}}_{\mathbf{u}} \mathbf{F}_{u_r} \right) \right]^T (\mathbf{\Theta}_{x,r} \otimes \mathbf{T}_{y_j}) \right\}, \tag{3.27}$$

where, $\bar{\mathbf{E}}_{\mathbf{u}} = \mathbf{I}_K - \mathbf{W}_R \mathbf{H}_u - \mathbf{W}_R \mathbf{G}_u \text{Diag}(\mathbf{\Phi}) \mathbf{F}_u$ and $\mathbf{T}_{z_m}$ is a $M_z \times M_z$ sparse matrix with 1 as its m^{th} diagonal element and 0 elsewhere. Here, $z \in \{x, y\}$. Once the gradient is found, the new phase shift vectors of each of the IRS is updated as in (3.28):

$$\mathbf{\Phi}_{z_r}^{t+1} = \mathbf{\Phi}_{z_r}^{t} - \mu \left[\frac{\partial E_u}{\partial \mathbf{\Phi}_{z_r}} \right]^*, \tag{3.28}$$

where μ is the predefined step size which is varying to ensure the optimal point is reached. When the change in the objective value becomes smaller than a predefined value, the step size is reduced to guarantee convergence. In (3.28), $\mathbf{\Phi}_{z_r}^t$ denotes the phase shift vector at the t^{th} iteration. Having calculated the new phase-shift vectors, the result is projected back to the feasible region using the following projection function:

$$[\mathbf{\Phi}_{z_r}]_{(m)} = \frac{[\mathbf{\Phi}_{z_r}]_{(m)}}{|[\mathbf{\Phi}_{z_r}]_{(m)}|}. \tag{3.29}$$

The projection function in (3.29) ensures that the solution remains within the feasible region defined by the constraint in (**??**). This procedure is carried out for all the IRSs and is repeated until the objective function converges, which is determined when the change in its value becomes smaller than a predefined accuracy threshold.

The overall steps for optimizing the uplink system are outlined in **Algorithm 2**.

3.4.2 Downlink Communication

To determine the optimal values for the variables in the downlink communication model, the problem in P3 must be solved. Here too, a multi-variable constrained problem is encountered, and therefore, an AO based method is employed to obtain the optimal solutions. This involves addressing the following two sub-problems:

$$\begin{aligned} \text{P31} : \arg\min_{\alpha,\mathbf{W}} \; & ||\alpha[\mathbf{H}_d + \mathbf{F}_d \text{Diag}(\mathbf{\Phi})\mathbf{G}_d]\mathbf{W} - \mathbf{I}_K||_F^2 \\ & + \sigma^2 \text{trace}(\alpha^2) \end{aligned} \tag{3.30a}$$

subject to

$$\text{C1} : ||\mathbf{W}||_F^2 \leq P_t, \tag{3.30b}$$

Algorithm 2 Joint Optimization of Linear Receiver Matrix and Phase-Shift Vectors of Uplink Transmission of the cell-free MIMO system

Initialize: initial iteration number $i = 0$, initial $\{\mathbf{\Phi}_x^0, \mathbf{\Phi}_y^0\}$, step size μ, accuracy level ϵ, step size related threshold ϵ_μ and maximum iteration number $I_{\max}$.

Generate the channels, $\mathbf{H}$, $\mathbf{G}$ and $\mathbf{F}$.

repeat

Set the iteration number $i \leftarrow i + 1$.

Compute $\mathbf{H}_t$ using (3.23).

Compute $\mathbf{W}_R$ using (3.24).

Compute the gradients of the objective function of P22 using (3.26) and (3.27).

Update the phase shift vectors using (3.28).

Project each element of $\mathbf{\Phi}_x^i$ and $\mathbf{\Phi}_y^i$ of each IRS with the projection function in (3.29)

Compute the objective based on the newly obtained values.

If $i \geq 2$ and the change in objective value is lesser than ϵ_μ, make $\mu = \mu/2$.

until Objective converges below the desired accuracy level ϵ or number of iterations exceeds $I_{\max}$.

return $\mathbf{W}_R, \mathbf{\Phi}_x$ and $\mathbf{\Phi}_y$.

$$\text{P32}: \underset{\boldsymbol{\Phi}_{x_r}, \boldsymbol{\Phi}_{y_r}}{\arg\min} \ \left\| \alpha[\mathbf{H}_d + \mathbf{F}_d \text{Diag}(\boldsymbol{\Phi}) \mathbf{G}_d] \mathbf{W} - \mathbf{I}_K \right\|_F^2 \tag{3.31a}$$

subject to

$$\text{C2}: |[\boldsymbol{\Phi}_{x_r}]_{(i)}| = 1, \ i = 1, 2, ..., M_x, \tag{3.31b}$$

$$\text{C3}: |[\boldsymbol{\Phi}_{y_r}]_{(j)}| = 1, \ j = 1, 2, ..., M_y. \tag{3.31c}$$

To find the optimal variable values, these two sub-problems are solved independently and iteratively until the objective function converges.

Receiver Scaling Factor (α) and BS Beamforming Matrix ($\mathbf{W}$) Optimization

To find the optimal receiver scaling factor, α^{opt} and the optimal beamforming matrix, $\mathbf{W}^{\text{opt}}$, the problem P31 is solved using the Lagrangian method. The Lagrangian function corresponding to the problem is formulated as in (3.32):

$$\begin{aligned} \mathcal{L}(\lambda, \alpha, \mathbf{W}) = \ & ||\alpha[\mathbf{H}_d + \mathbf{F}_d \text{Diag}(\boldsymbol{\Phi}) \mathbf{G}_d] \mathbf{W} - \mathbf{I}_K||_F^2 \\ & + \sigma^2 \text{trace}(\alpha^2) + \lambda \left(||\mathbf{W}||_F^2 - P_t \right), \end{aligned} \tag{3.32}$$

where λ is the Lagrange multiplier corresponding to the constraint in (3.30b). The partial derivatives of the Lagrangian function with respect to the two optimization variables and λ are set to zero to obtain the optimal values for α and $\mathbf{W}$ shown in (3.33) and (3.34):

$$\alpha^{\text{opt}} = \sqrt{\frac{1}{P_t}} \sqrt{\text{Tr}\left[\left(\mathbf{H}^H \mathbf{H} + \frac{K \sigma^2 \mathbf{I}_{NB}}{P_t} \right)^{-2} \mathbf{H}^H \mathbf{H} \right]}, \tag{3.33}$$

$$\mathbf{W}^{\text{opt}} = \frac{\sqrt{P_t} \left[\mathbf{H}^H \mathbf{H} + \frac{K \sigma_w^2 \mathbf{I}_{NB}}{P_t} \right]^{-1} \mathbf{H}^H}{\sqrt{\text{Tr}\left[(\mathbf{H}^H \mathbf{H} + \frac{K \sigma^2 \mathbf{I}_N}{P_t})^{-2} \mathbf{H}^H \mathbf{H} \right]}},$$

$$\mathbf{W}^{\text{opt}} = \alpha^{\text{opt}^{-1}} \left[\mathbf{H}^H \mathbf{H} + \frac{K\sigma^2 \mathbf{I}_{NB}}{P_t} \right]^{-1} \mathbf{H}^H. \tag{3.34}$$

In the above equations,

$$\mathbf{H} = \mathbf{H}_d + \mathbf{F}_d \text{Diag}(\mathbf{\Phi}) \mathbf{G}_d, \tag{3.35}$$

where $\mathbf{H}$ is the total channel matrix of the downlink communication system.

Optimization of Phase Shift Vectors ($\mathbf{\Phi}_{x_r}$ and $\mathbf{\Phi}_{y_r}$)

The same approach of projected gradient descent is followed to solve the problem in P32 which was used in the uplink communication problem. For the easiness of representation and calculation of the gradients, the objective function is first re-arranged as follows:

$$E_d = \left\| \alpha \left(\mathbf{H}_d + \sum_{r=1}^{R} \mathbf{F}_{d_r} \text{Diag}(\mathbf{\Phi}_{x_r} \otimes \mathbf{\Phi}_{y_r}) \mathbf{G}_{d_r} \right) - \mathbf{I}_K \right\|_F^2. \tag{3.36}$$

The gradient is calculated with respect to each of the elements in the phase shift vectors as follows:

$$\frac{\partial E_d}{\partial [\mathbf{\Phi}_{x_r}]_{(i)}} = 2\alpha \text{Tr} \left\{ \left[\text{Re} \left(\mathbf{F}_{d_r}^H \bar{\mathbf{E}}_{\mathbf{d}} \mathbf{G}_{d_r} \right) \right]^T (\mathbf{T}_{x_i} \otimes \mathbf{\Theta}_{y_r}) \right\}, \tag{3.37}$$

$$\frac{\partial E_d}{\partial [\mathbf{\Phi}_{y_r}]_{(j)}} = 2\alpha \text{Tr} \left\{ \left[\text{Re} \left(\mathbf{F}_{d_r}^H \bar{\mathbf{E}}_{\mathbf{d}} \mathbf{G}_{d_r} \right) \right]^T (\mathbf{\Theta}_{x_r} \otimes \mathbf{T}_{y_j}) \right\}, \tag{3.38}$$

where

$$\bar{\mathbf{E}}_{\mathbf{d}} = \alpha \mathbf{H} \mathbf{W} - \mathbf{I}_K, \tag{3.39}$$

with $\mathbf{H}$ given in (3.35) and $\mathbf{T}_{z_m}$ is a $M_z \times M_z$ sparse matrix with 1 as its m^{th} diagonal element and 0 elsewhere for $z \in \{x, y\}$. The new phase-shift vectors of each IRS are found using (3.28) and by projecting the obtained result with (3.29), the new phase-shift vectors are ensured to be in the feasible region of the considered problem.

The overall procedure of the downlink communication optimization is shown step-by-step in **Algorithm 3**.

Algorithm 3 Joint Optimization of Receiver Scaling Factor, Beamforming Matrix and Phase-Shift Vectors of Downlink Transmission of the cell-free MIMO system

Initialize: initial iteration number $i = 0$, initial $\{\mathbf{\Phi}_x^0, \mathbf{\Phi}_y^0\}$, step size μ, accuracy level ϵ, step size related threshold ϵ_μ and maximum iteration number $I_{\max}$.

Generate the channels, $\mathbf{H}$, $\mathbf{G}$ and $\mathbf{F}$.

repeat

Set the iteration number $i \leftarrow i + 1$.

Compute $\mathbf{H}$ using (3.35).

Compute α^{opt} using (3.33).

Compute $\mathbf{W}$ using (3.34).

Compute the gradients of the objective function of P32 using (3.37) and (3.38).

Update the phase shift vectors using (3.28).

Project each element of $\mathbf{\Phi}_x^i$ and $\mathbf{\Phi}_y^i$ of each IRS with the projection function in (3.29)

Compute the objective based on the newly obtained values.

If $i \geq 2$ and the change in objective value is lesser than ϵ_μ, make $\mu = \mu/2$.

until Objective converges below the desired accuracy level ϵ or number of iterations exceeds $I_{\max}$.

return $\mathbf{W}_R, \mathbf{\Phi}_x$ and $\mathbf{\Phi}_y$.

3.4.3 Complexity Analysis

The computational complexity of both the uplink and downlink algorithms is primarily determined by two operations. First, the calculation of the optimal linear receiver matrix in the uplink system and the optimal receiver scaling factor and beamforming matrix in the downlink system involves the inversion of a matrix of size $NB \times NB$, which results in a complexity of $\mathcal{O}((NB)^3)$. Second, the gradient computation required for the gradient descent algorithm in both cases incurs a complexity of $\mathcal{O}((MR)^2)$. Consequently, the overall computational complexity of the uplink and downlink algorithms is $\mathcal{O}((NB)^3 + ((MR)^2))$, where the dominant term depends on the relative magnitudes of NB and MR.

3.5 Numerical Results

3.5.1 Simulation Parameters

This section presents Monte Carlo simulation results to evaluate the performance of IRSs with Kronecker-based phase shift matrices in a cell-free network. The experiments were conducted using 3 BSs, 2 Kronecker IRSs, and 12 users. Each BS was equipped with 12 antennas for either reception or transmission, depending on whether uplink or downlink communication was considered. Each IRS consisted of 144 elements arranged in a 12×12 grid.

The distance between each BS and user was randomly selected from a uniform distribution between 400 m and 600 m, while the user-IRS distance followed a uniform distribution ranging from 10 m to 50 m. The IRSs were positioned 500 m away from two BSs and 600 m from the third. For channel generation, the reference distance d_0 was set to 1 m, with a pathloss at d_0, C_0, assumed to be -30 dB. The path-loss exponents, η for the BS-user, BS-IRS, and IRS-user channels were set to 3.7, 2.5, and 2.5, respectively,

with the number of channel paths, Q set to 2, 8, and 2, respectively. The channel path gains, denoted by c_q for all three types of channels are modeled as complex Gaussian random variables with zero mean and unit variance.

In the uplink communication model, the transmit power of each user is set to 1 dBm, while in the downlink model, each BS transmits at 10 dBm. The noise variance is assumed to be -100 dBm.

3.5.2 Performance Analysis

To assess the effectiveness of the Kronecker-based IRS control method in cell-free networks, sum-rate and good-put are considered as the two key metrics. These metrics are used to compare the proposed approach with two alternative IRS control strategies as used in Chapter 2. The first, known as the Conventional IRS model, adjusts the phase shifts of individual IRS elements independently. The second method applies random phase shifts to the IRS elements without any optimization. Furthermore, the analysis explores how critical system parameters influence performance based on these metrics. Specifically, the study examines the impact of the number of IRS elements per IRS, the transmit power of users/ base stations, and the total number of users on overall system performance.

Sum-Rate in the Uplink System

The uplink sum-rate in a cell-free MIMO system represents the total data transmission capacity from all users to the distributed BSs within the network, capturing the combined effects of channel conditions and user distribution. The sum-rate of the uplink cell-free system is calculated as shown in (3.40):

$$R_u = \log_2 \left| \mathbf{I}_{NB} + \frac{P \mathbf{H}_t \mathbf{H}_t^H}{\sigma^2} \right|, \tag{3.40}$$

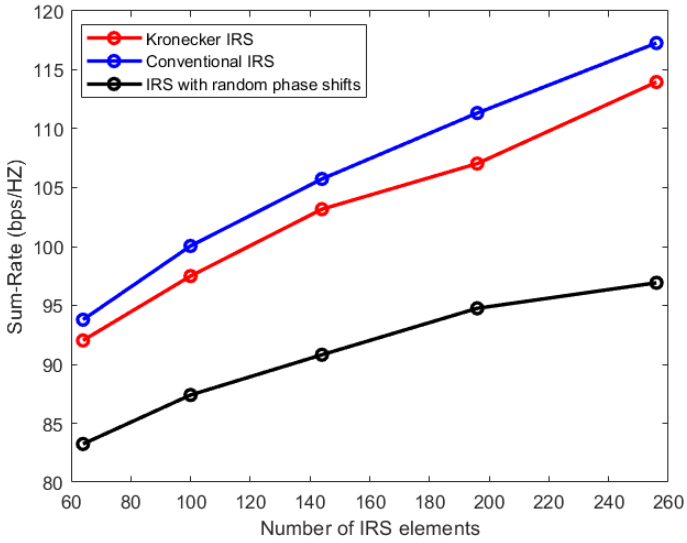

Figure 3.2: Sum-rate variation of the uplink system with the number of IRS elements (K = 12, P = 1 dBm)

where $\mathbf{H}_t$ is given by (3.23). The term $\mathbf{H}_t\mathbf{H}_t^H$ captures both the power of the users' signals and the interference between them, as it represents how the users' channels interact with each other. The diagonal entries mainly represent the strength of each user's own signal, while the off-diagonal entries show the interference caused by other users.

This approach assumes that the BSs work together to process all users' signals centrally, which helps to manage interference by using the distributed antennas effectively. Moreover, σ^2 represents the power of the AWGN which is assumed to be constant across all antennas and frequency bands. It accounts for the thermal noise and other random disturbances in the system that degrade the signal quality.

Increasing the number of IRS elements in a cell-free MIMO system generally enhances the uplink sum-rate by providing finer control over the reflected signals. With more IRS elements, the system can achieve better phase alignment, improving signal

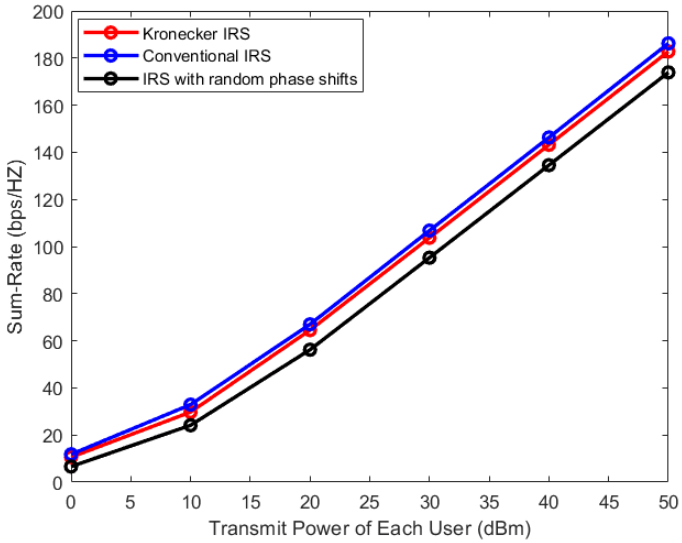

Figure 3.3: Sum-rate variation of the uplink system with the transmit power (K = 12, M = 144)

strength at the access points and reducing interference. This creates a more favorable propagation environment, increasing the effective channel gain for users. Additionally, the higher degree of freedom offered by additional elements enables more efficient resource allocation, further boosting the uplink sum-rate. This is reflected in Fig. 3.2, which illustrates the performance improvement as the number of IRS elements increases.

The effect of increasing the transmit power of each user on the uplink sum-rate is depicted in Fig. 3.3. Accordingly, as the transmit power increases, the sum-rate also rises due to the enhanced signal strength received at the access points.

Fig. 3.4 depicts the impact of increasing the number of users in the uplink system on the sum-rate. Generally, as the number of users increases, the sum-rate improves due to the higher cumulative data contribution. However, this gain depends on the system's ability to manage interference effectively, which relies on IRS phase shift optimization.

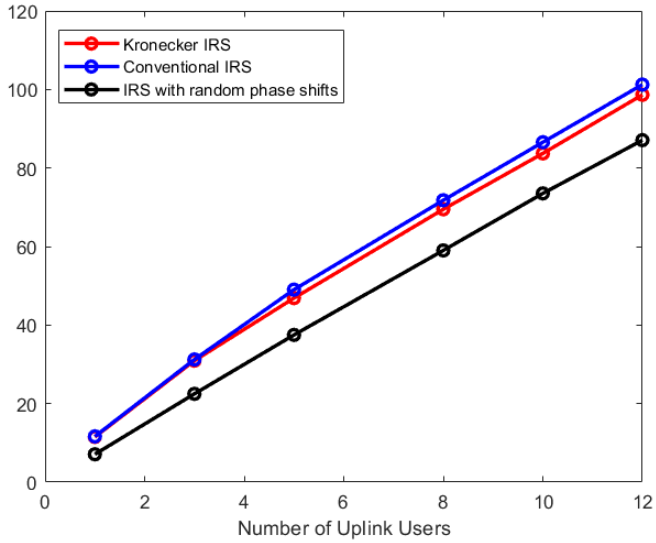

Figure 3.4: Sum-rate variation of the uplink system with the number of uplink users (P = 1 dBm, M = 144)

The IRS with random phase shifts consistently yields the lowest sum-rate, as the unoptimized phase alignment leads to inefficient signal reflection and higher interference. Among the optimized methods across all scenarios, the conventional model demonstrates a slightly higher sum-rate than the Kronecker-based model. However, the difference is relatively small, emphasizing that the Kronecker model, despite its reduced degrees of freedom in optimization, maintains competitive performance while offering potential advantages in computational complexity.

Sum-Rate in the Downlink System

The downlink sum-rate refers to the total data rate (or capacity) that can be transmitted from the BSs to multiple users in a wireless communication network. As the downlink sum-rate is often expressed as the sum of the individual rates at which each user can

receive data from the BS, the sum-rate of the downlink system is calculated as follows:

$$R_d = \sum_{k=1}^{K} \log_2 \left(1 + \frac{|\,[\mathbf{HW}]\,|^2_{(k,k)}}{\sum_{j \neq k} |\,[\mathbf{HW}]\,|^2_{(k,j)} + \alpha^2 \sigma^2} \right), \tag{3.41}$$

where $\mathbf{H}$ is given in (3.35) and $\mathbf{W}$ is the beamforming matrix. In this model, interference arises when signals intended for multiple users overlap due to the shared transmission resources and the distributed nature of the BSs. Here, each user not only receives their desired signal but also experiences interference from signals intended for other users, caused by the non-orthogonality of channels and imperfect beamforming. The interference power is modeled as the sum of the unintended signal components received by each user.

In the downlink scenario, the number of IRS elements plays a crucial role in enhancing the sum-rate. As the number of IRS elements increases, the system benefits from more precise beamforming capabilities, allowing the access point to focus the transmitted signal more effectively toward the intended users. This leads to a significant improvement in the SINR, which is critical for increasing the downlink sum-rate. The results, shown in Fig. 3.5, confirm that a larger IRS improves signal delivery, with the conventional model achieving the highest sum-rate. The Kronecker-based model, although slightly lower in performance, demonstrates a very small difference from the conventional approach, underscoring its potential as a viable alternative. On the other hand, the IRS with random phase shifts shows significantly lower performance, as expected, due to the un-optimized phase alignment that results in inefficient signal reflection and higher interference.

The transmit power also significantly influences the downlink sum-rate, as illustrated in Fig. 3.6. As the transmit power increases, the downlink sum-rate improves due to stronger signal strength at the user end. However, the magnitude of this improvement is closely tied to the efficiency of IRS phase shift optimization. The model with random phase shifts continues to exhibit the lowest sum-rate, confirming that without

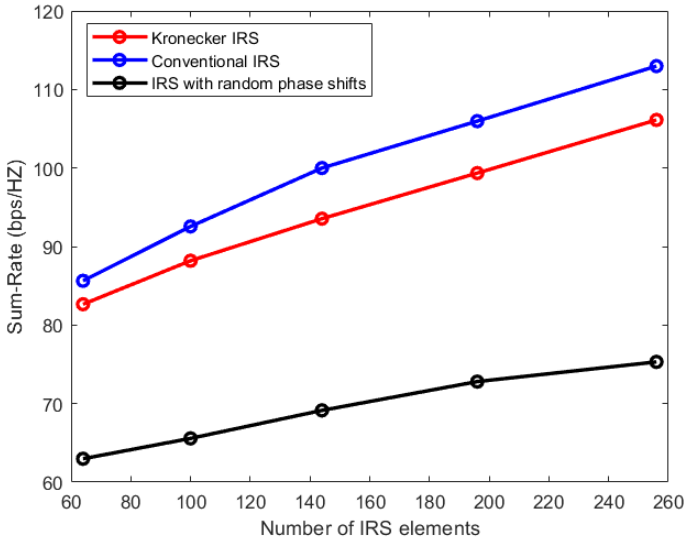

Figure 3.5: Sum-rate variation of the downlink system with the number of IRS elements (K = 12, P = 1 dBm)

optimized phase alignment, the system cannot achieve optimal signal focusing, even with higher transmit power. Both the conventional and Kronecker-based models show considerable improvement with increased transmit power, with the Kronecker model closely approaching the performance of the conventional model, but with a slightly lower sum-rate.

Finally, the effect of increasing the number of users in the downlink system is shown in Fig. 3.7. As the user population grows, the total downlink sum-rate generally increases, reflecting the higher data demand across the network. However, this increase is contingent on the system's ability to manage interference. In particular, the IRS's ability to direct signals efficiently and suppress interference becomes paramount. As observed, the conventional model continues to outperform the Kronecker-based model by a small margin, although the difference is minimal. This highlights the Kronecker model's robustness as an alternative with lower computational complexity, capable of

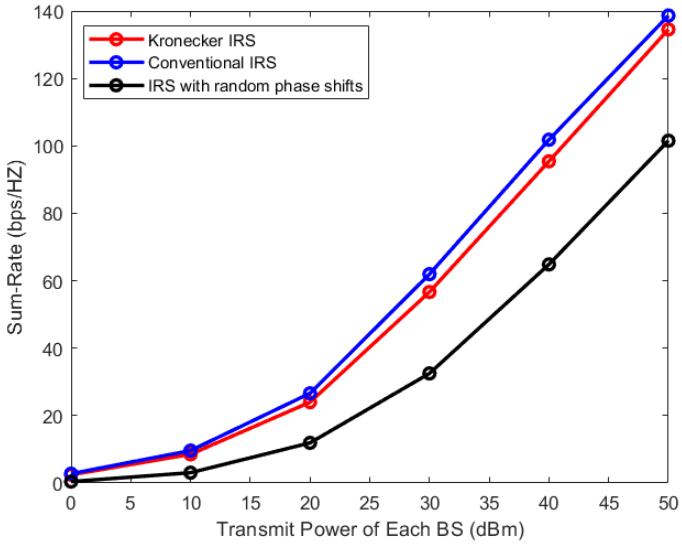

Figure 3.6: Sum-rate variation of the downlink system with the transmit power (K = 12, M = 144)

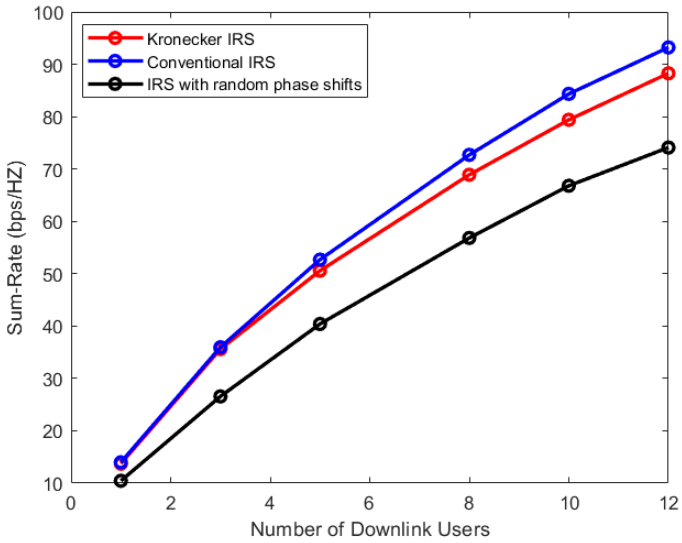

Figure 3.7: Sum-rate variation of the downlink system with the number of downlink users (P = 1 dBm, M = 144)

delivering near-conventional performance.

Across all three scenarios the results for the downlink sum-rate show a similar trend to the uplink case. The conventional model achieves the highest sum-rate, with the Kronecker model offering competitive performance. The random phase shift model consistently under-performs due to its inability to align phase shifts for optimal signal delivery, reinforcing the importance of phase optimization in both uplink and downlink scenarios.

Good-put in the Uplink System

The concept of good-put, which focuses on the amount of useful data transmitted per unit time, accounts for control overhead, retransmissions, and other non-useful data. In the context of the uplink cell-free MIMO system, the good-put is calculated as follows [63]:

$$GP_u = \left(1 - \frac{bM_{IRS}}{\eta N_s}\right) R_u, \tag{3.42}$$

where R_u denotes the sum-rate which is calculated using by (3.40). The term inside the bracket in (3.42) accounts for the control overhead of the network and the parameters are explained in Section 2.6.2. For the simulations, the parameters are set as follows: $b = 4$ bits per IRS element per time slot, $\eta = 4$ bits per second per Hertz (bps/Hz), and $N_s = 1000$ symbols per slot. Note that for the system with Kronecker-based IRSs, the number of IRS elements is given by $M_{IRS} = R(M_x + M_y)$, while for with conventional IRSs, it is $M_{IRS} = R(M_x \times M_y)$. Additionally, for IRS configurations where random phase shifts are assigned, the good-put coincides with the sum-rate, as no signals for controlling the phase shifts are involved.

The effects of three key factors on the system's good-put performance: the number of elements in each IRS, the transmit power, and the number of users in the network are analyzed. These effects are illustrated in Fig. 3.8, Fig. 3.9 and Fig. 3.10, respectively.

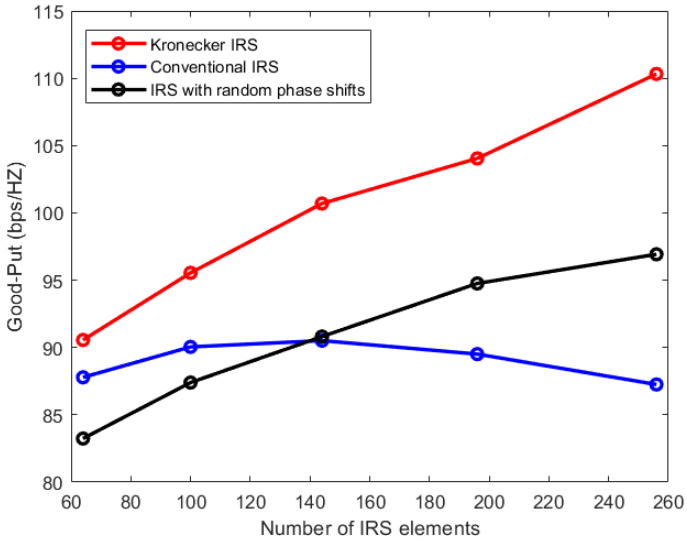

Figure 3.8: Good-put variation of the uplink system with the number of IRS elements in each IRS (K = 12, P = 1 dBm)

The results indicate that the Kronecker-based IRS model consistently outperforms the other two methods across all scenarios, demonstrating a significantly higher good-put. This improvement is attributed to the efficient control structure of the Kronecker-based model, which requires fewer control signals compared to the conventional IRS.

For the conventional IRS model, the good-put demonstrates a rapid decline as the number of IRS elements grows. Remarkably, its performance eventually falls below that of the random phase shift model. This decline is attributed to the significant control signaling overhead required to manage a large number of IRS elements, which outweighs the benefits of improved beamforming. In contrast, the IRS model with random phase shifts consistently exhibits the lowest good-put in the initial range, as expected, due to its inability to align with the channel conditions and optimize signal reflection effectively. However, as the number of IRS elements increases, the random phase shift model avoids the control signaling overhead entirely, allowing its good-put to remain comparable to

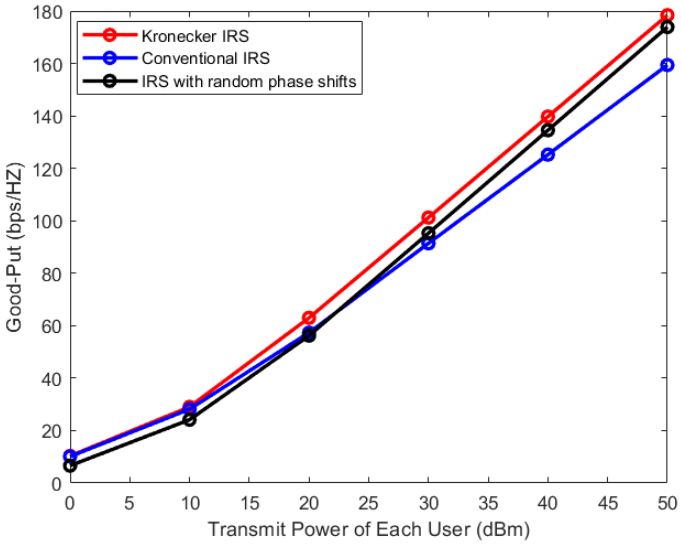

Figure 3.9: Good-put variation of the uplink system with the transmit power of each uplink user (K = 12, M = 144)

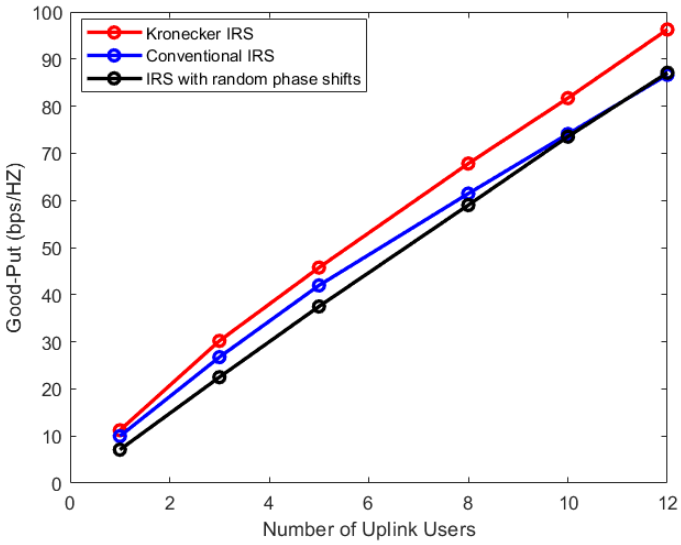

Figure 3.10: Good-put variation of the uplink system with the number of uplink users (P = 1 dBm, M = 144)

its sum-rate and surpassing the conventional model at high element counts.

With all three models, the good-put demonstrates an increasing trend with transmit power and the number of users. A higher transmit power enhances the SINR, thereby improving spectral efficiency and achievable rates. Similarly, increasing the number of users benefits from the distributed nature of cell-free MIMO systems, where the system can efficiently manage user demands through collaborative processing across access points.

Good-put in the Downlink System

Similar to the uplink case, the performance of the downlink cell-free model is evaluated using the good-put. The good-put of the downlink system is calculated by

$$GP_d = \left(1 - \frac{bM_{IRS}}{\eta N_s}\right) R_d, \tag{3.43}$$

where R_d is the downlink sum-rate calculated as in (3.41). The remaining parameters in (3.43) are similar to those defined in the Section 2.6.2.

The effects of the number of IRS elements, transmit power, and the number of users on system good-put were evaluated, similar to the uplink case. As shown in Fig. 3.11, Fig. 3.12 and Fig. 3.13, the Kronecker-based IRS model outperforms the conventional IRS and random phase shift models in all scenarios. The good-put of the Kronecker-based model increases consistently, while the conventional IRS experiences a decline as the number of elements increases due to higher control signaling overhead. The IRS with random phase shifts shows the lowest good-put in all cases, as expected, due to its inability to optimize signal reflection. Overall, the good-put trends follow the same pattern as in the uplink case, where transmit power and the number of users improve performance.

In conclusion, the Kronecker-based model demonstrates superior performance by effectively mitigating the small sum-rate loss due to control overhead. Its reduced sig-

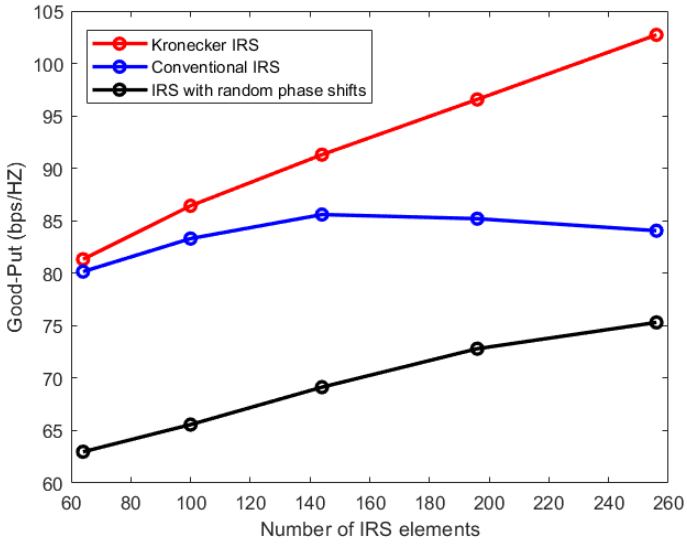

Figure 3.11: Good-put variation of the downlink system with the number of IRS elements (K = 12, P = 1 dBm)

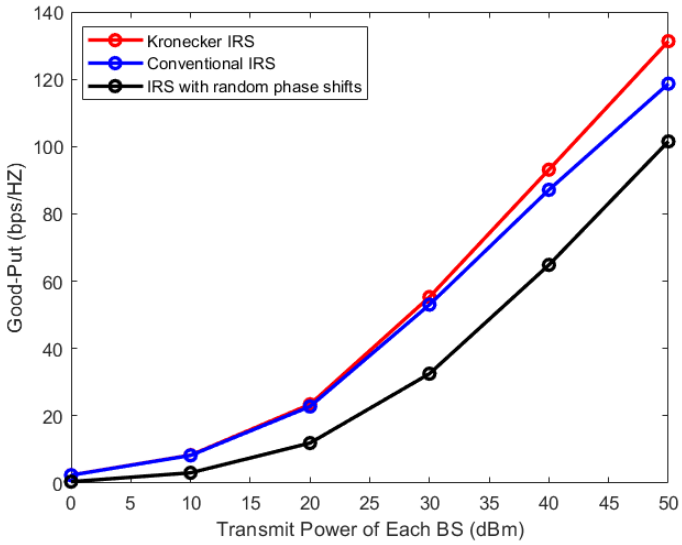

Figure 3.12: Good-put variation of the downlink system with the transmit power (K = 12, M = 144)

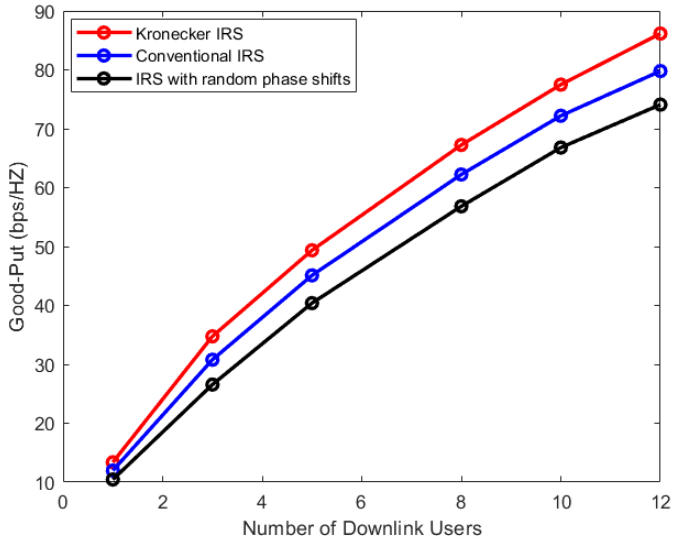

Figure 3.13: Good-put variation of the downlink system with the number of downlink users (P = 1 dBm, M = 144)

naling requirements, in contrast to the conventional IRS, make it a more efficient and practical solution for controlling IRS elements. By striking an optimal balance between control complexity and system performance, the Kronecker model ensures better overall good-put, while the conventional IRS faces significant overhead as the number of elements increases. Thus, the Kronecker-based model can be introduced as a more suitable approach for optimizing IRS-assisted wireless systems including cell-free MIMO systems.

3.6 Conclusion

This chapter has presented an in-depth evaluation of the Kronecker-based phase shift matrix for controlling IRS in the context of cell-free MIMO systems. Focusing on the MMSE criterion, both the uplink and downlink systems have been optimized to enhance

network performance. Specifically, the linear receiver matrix and phase shift matrix in the uplink communication system, and the beamforming matrix and phase shift vectors in the downlink communication model have been optimized. The performance of the Kronecker model has been tested, and it has been demonstrated that this model effectively reduces control overhead while maintaining superior performance compared to conventional IRS model where phase shifts of elements are controlled individually. Despite a small sum-rate loss due to control overhead, the Kronecker model requires fewer signaling resources and consistently outperforms other methods in terms of good-put, in contrast to the conventional IRS which suffers from increased overhead as the number of elements grows and the random phase-shift models that show inferior performance due to inefficient signal reflections.

Overall, the findings validate that the Kronecker-based model works well in cell-free systems and offers a promising solution for optimizing IRS-assisted wireless communication networks.

Chapter 4

Conclusion and Future Directions

4.1 Concluding Remarks

This thesis presented a comprehensive study of IRSs in wireless communication networks, introducing a novel Kronecker-based method to optimize their phase shift control to enhance system performance. Two key systems were investigated: a simple downlink transmission network and a more complex cell-free MIMO system. The findings of this research contribute to the growing understanding of IRS technology and its potential to revolutionize wireless networks.

In the second chapter, the Kronecker-based phase shift control method was introduced and validated within the context of a simple downlink transmission system. By leveraging the Kronecker product, this approach effectively reduced the number of control signals required to optimize the IRS phase shifts, while maintaining system performance. An optimization problem was formulated based on the MMSE criterion and solved using an AO framework. Numerical results demonstrated that the proposed Kronecker-based method outperformed traditional element-wise phase shift control, offering a practical and scalable solution for IRS deployment in simpler network settings.

The third chapter extended the Kronecker-based phase shift model to cell-free MIMO systems, which represent a cutting-edge approach to wireless communication. This system model incorporated multiple IRSs to further enhance signal propagation, improve coverage, and mitigate interference. Optimization problems were formulated for both uplink and downlink communication, focusing on joint optimization of IRS phase shifts and beamforming or receiver matrices at distributed BSs. The performance of the proposed system was analyzed using metrics such as sum-rate and good-put, and numerical simulations validated the efficiency of the Kronecker-based method in reducing control overhead and enhancing network performance in complex, distributed environments.

Overall, this thesis demonstrates the versatility and efficiency of the Kronecker-based IRS control method, showcasing its potential for deployment in both simple and advanced wireless communication systems. The findings highlight the importance of intelligent IRS phase shift control in improving signal quality, reducing interference, and optimizing energy efficiency, making it a promising approach for the next generation of wireless networks.

4.2 Future Directions

Future directions of this research work include, but are not limited to, the following.

4.2.1 Analysis of the Control Method with Stacked Intelligent Metasurfaces (SIMs)

Investigating the application of the Kronecker-based IRS control method to stacked intelligent metasurfaces (SIMs) could provide additional degrees of freedom in phase control, enhancing signal manipulation and network performance. Extending this approach to multi-layer metasurfaces may further reduce control overhead while improving

system efficiency in both cell-based and cell-free networks.

4.2.2 Application to User-Centric Architectures

Exploring the use of IRSs in user-centric cell-free MIMO architectures, where the system dynamically groups BSs and IRSs to optimize service quality for individual users could further enhance the adaptability of the system to user-specific needs.

4.2.3 Dynamic IRS Control for Real-Time Applications

Extending the proposed Kronecker-based model to dynamic environments where user locations, channel conditions, and network topology change frequently and investigating real-time IRS control algorithms that adapt to these variations while maintaining low complexity can be a promising avenue for future research.

4.2.4 Integration with 6G Technologies

Exploring the integration of the Kronecker-based IRS control method with emerging 6G technologies such as terahertz communication, intelligent beam management, and AI-driven network optimization could uncover new use cases and enhance the scalability of IRSs in ultra-dense networks.

4.2.5 Energy Efficiency in Large-Scale Deployments in Cell-Free Networks

Analyzing the energy efficiency of IRS deployments in cell-free systems, considering factors such as power consumption of IRS controllers and distributed BSs and developing power-efficient hardware and optimization methods could contribute to greener communication networks.

4.2.6 Interference Management in Multi-Cell Networks

Investigating the application of the Kronecker-based method in multi-cell networks where interference from neighboring cells becomes significant and designing cooperative strategies among IRSs and BSs could help mitigate inter-cell interference.

4.2.7 Robustness to Imperfect CSI

Extending the current optimization framework to scenarios with imperfect CSI, employing robust optimization techniques to handle uncertainties in channel estimation, which are inevitable in practical systems.

4.2.8 Experimentation with Hardware Prototypes

Validating the proposed methods using hardware prototypes and testbeds to bridge the gap between theoretical research and practical implementation, involving designing IRS elements with real-world constraints, such as phase quantization and limited resolution.

Bibliography

[1] M. Islam and S. Jin, "An overview research on wireless communication network," vol. 5, p. 10, 09 2019.

[2] O. Oladele, "Advances in wireless network technologies and their impact on computer science applications," 09 2024.

[3] I. F. Akyildiz, A. Kak, and S. Nie, "6g and beyond: The future of wireless communications systems," *IEEE access*, vol. 8, pp. 133995–134030, 2020.

[4] R. Dangi, P. Lalwani, G. Choudhary, I. You, and G. Pau, "Study and investigation on 5g technology: A systematic review," *Sensors (Basel, Switzerland)*, vol. 22, no. 1, pp. 26–, 2021.

[5] I. Ahmad, F. Osasona, S. Dawodu, O. Obi, A. Anyanwu, and S. Onwusinkwue, "Emerging 5g technology: A review of its far-reaching implications for communication and security," *World Journal of Advanced Research and Reviews*, vol. 21, pp. 2474–2486, 01 2024.

[6] S. Hussain, N. Bhadri, and S. Hussain, "Advancements in wireless communication," 09 2020.

[7] N. Titus and K. P. Extension, "The impact of 5g technology on autonomous vehicles," vol. 3, pp. 36–39, 09 2024.

[8] M. Javaid, A. Haleem, R. P. Singh, and R. Suman, "5g technology for healthcare: Features, serviceable pillars, and applications," *Intelligent Pharmacy*, vol. 1, no. 1, pp. 2–10, 2023.

[9] A. Gohar and G. Nencioni, "The role of 5g technologies in a smart city: The case for intelligent transportation system," *Sustainability*, vol. 13, no. 9, pp. 5188–, 2021.

[10] H. Ganame, L. Yingzhuang, H. Ghazzai, and D. Kamissoko, "5g base station deployment perspectives in millimeter wave frequencies using meta-heuristic algorithms," *Electronics*, vol. 8, no. 11, 2019.

[11] A. Ashraf, T. Gunawan, M. Kartiwi, L. Nur, B. Nugroho, and R. Pudji Astuti, "Advancements and challenges in scalable modular antenna arrays for 5g massive mimo networks," *IEEE Access*, vol. PP, pp. 1–1, 01 2024.

[12] M. Ajmal, A. Siddiqa, B. Jeong, J. Seo, and D. Kim, "Cell-free massive multiple-input multiple-output challenges and opportunities: A survey," *ICT Express*, vol. 10, no. 1, pp. 194–212, 2024.

[13] M. Mohammadi, Z. Mobini, H. Ngo, and M. Matthaiou, "Next generation multiple access with cell-free massive mimo," 11 2023.

[14] M. Mohammadi, Z. Mobini, H. Q. Ngo, and M. Matthaiou, "Next generation multiple access with cell-free massive mimo," 2024.

[15] S. Elhoushy, M. Ibrahim, and W. Hamouda, "Cell-free massive mimo: A survey," *IEEE Communications Surveys & Tutorials*, vol. 24, no. 1, pp. 492–523, 2021.

[16] Q. Wu and R. Zhang, "Towards smart and reconfigurable environment: Intelligent reflecting surface aided wireless network," *arXiv.org*, 2019.

[17] K. Qu, K. Chen, J. Zhao, N. Zhang, Q. Hu, J. Zhao, T. Jiang, and Y. Feng, "An electromechanically reconfigurable intelligent surface for enhancing sub-6g wireless communication signal," *Journal of Information and Intelligence*, vol. 1, no. 3, pp. 207–216, 2023.

[18] X. Yuan, Y.-J. A. Zhang, Y. Shi, W. Yan, and H. Liu, "Reconfigurable-intelligent-surface empowered wireless communications: Challenges and opportunities," *IEEE Wireless Communications*, vol. 28, no. 2, pp. 136–143, 2021.

[19] C. Huang, A. Zappone, G. C. Alexandropoulos, M. Debbah, and C. Yuen, "Reconfigurable intelligent surfaces for energy efficiency in wireless communication," *IEEE Transactions on Wireless Communications*, vol. 18, no. 8, pp. 4157–4170, 2019.

[20] Q. Wu and R. Zhang, "Intelligent reflecting surface enhanced wireless network: Joint active and passive beamforming design," in *2018 IEEE Global Communications Conference (GLOBECOM)*, pp. 1–6, IEEE, 2018.

[21] T. Sharma, A. Chehri, and P. Fortier, "Reconfigurable intelligent surfaces for 5g and beyond wireless communications: A comprehensive survey," *Energies (Basel)*, vol. 14, no. 24, pp. 8219–, 2021.

[22] D. L. Galappaththige, D. Kudathanthirige, and G. Amarasuriya, "Performance analysis of irs-assisted cell-free communication," 2021.

[23] K. Wang, N. Qi, X. Guan, Q. Shi, M. Xiao, S. Jin, and K.-K. Wong, "Transmit/passive beamforming design for multi-irs assisted cell-free mimo networks," *IEEE Systems Journal*, vol. 17, no. 4, pp. 6282–6291, 2023.

[24] R. Kumar, S. K. Gupta, H.-C. Wang, C. S. Kumari, and S. S. V. P. Korlam, "From efficiency to sustainability: Exploring the potential of 6g for a greener future," *Sustainability*, vol. 15, no. 23, pp. 16387–, 2023.

[25] P. Serrano, A. de la Oliva, P. Patras, V. Mancuso, and A. Banchs, "Greening wireless communications: Status and future directions," *Computer Communications*, vol. 35, no. 14, pp. 1651–1661, 2012. Special issue: Wireless Green Communications and Networking.

[26] T. Nikolic, M. Stojcev, G. Nikolic, and G. Jovanović, "Energy harvesting techniques in wireless sensor networks," *Facta Universitatis, Series: Automatic Control and Robotics*, vol. 17, p. 117, 12 2018.

[27] S. Mekid, A.-u.-d. Qureshi, and U. Baroudi, "Energy harvesting from ambient radio frequency: Is it worth it?," *Arabian Journal for Science and Engineering*, vol. 42, 09 2016.

[28] K. Muppavaram, S. Govathoti, D. Kamidi, and B. T, "Exploring the generations: A comparative study of mobile technology from 1g to 5g," *International Journal of Electronics and Communication Engineering*, vol. 10, pp. 54–62, 07 2023.

[29] A. Papazafeiropoulos, P. Kourtessis, M. D. Renzo, S. Chatzinotas, and J. M. Senior, "Performance analysis of cell-free massive mimo systems: A stochastic geometry approach," *IEEE Transactions on Vehicular Technology*, vol. 69, no. 4, pp. 3523–3537, 2020.

[30] S. Fukue, H. Iimori, G. T. F. De Abreu, and K. Ishibashi, "Joint access configuration and beamforming for cell-free massive mimo systems with dynamic tdd," *IEEE Access*, vol. 10, pp. 40130–40149, 2022.

[31] H. Ngo, L.-N. Tran, T. Duong, M. Matthaiou, and E. Larsson, "On the total energy efficiency of cell-free massive mimo," 02 2017.

[32] S. Kim and B. Shim, "Energy-efficient millimeter-wave cell-free systems under limited feedback," *IEEE Transactions on Communications*, vol. 69, pp. 4067–4082, 02 2021.

[33] A. Adewumi, F. Chizea, and B. Ayantunji, "Network and complex systems a review of cellular networks: Applications, benefits and limitations," vol. vol. 11, 12 2020.

[34] K. Shen and W. Yu, "Coordinated uplink scheduling and beamforming for wireless cellular networks via sum-of-ratio programming and matching," in *2016 IEEE International Conference on Acoustics, Speech and Signal Processing (ICASSP)*, pp. 3531–3535, 2016.

[35] H. Dahrouj and W. Yu, "Coordinated beamforming for the multi-cell multi-antenna wireless system," in *2008 42nd Annual Conference on Information Sciences and Systems*, pp. 429–434, IEEE, 2008.

[36] N. Trabelsi, L. Chaari Fourati, and C. S. Chen, "Interference management in 5g and beyond networks: A comprehensive survey," *Computer Networks*, vol. 239, p. 110159, 2024.

[37] B. Romanous, N. Bitar, M. Imran, and H. Refai, "Network densification: Challenges and opportunities in enabling 5g," 09 2015.

[38] Y. Xiaohu, D. Wang, and J. Wang, *Fundamentals of Distributed MIMO and Cell-Free Mobile Communications*, pp. 1–13. 01 2021.

[39] X. You, D. Wang, and J. Wang, *Distributed MIMO and cell-free mobile communication*. Singapore: Springer, 1st ed. 2021. ed., 2021.

[40] M. Z. Siddiqi, A. Munir, S. A. H. Mohsan, S. Shah, S. Chaudhary, P. Sangwongngam, and L. Wuttisittikulkij, "Low-complexity beamforming design for a cooperative reconfigurable intelligent surface-aided cell-free network," *Sensors*, vol. 23, no. 2, 2023.

[41] Y. Zhao, I. Niemegeers, and S. Heemstra de Groot, "Dynamic power allocation for cell-free massive mimo: Deep reinforcement learning methods," *IEEE Access*, vol. 9, pp. 102953–102965, 01 2021.

[42] W. Fan, J. Zhang, E. Björnson, S. Chen, and Z. Zhong, "Performance analysis of cell-free massive mimo over spatially correlated fading channels," pp. 1–6, 05 2019.

[43] H. Masoumi and M. Emadi, "Performance analysis of cell-free massive mimo system with limited fronthaul capacity and hardware impairments," *IEEE Transactions on Wireless Communications*, vol. PP, pp. 1–1, 11 2019.

[44] J. Zheng, J. Zhang, H. Du, D. Niyato, B. Ai, M. Debbah, and K. B. Letaief, "Mobile cell-free massive mimo: Challenges, solutions, and future directions," 2023.

[45] R. Roshanghias and R. Saadat, "Cluster-based cell-free massive mimo systems: A novel framework to enhance spectral efficiency with low complexity," 2023.

[46] G. Femenias and F. Riera-Palou, "Fronthaul-constrained cell-free massive mimo with low resolution adcs," *IEEE Access*, vol. 8, pp. 116195–116215, 2020.

[47] U. Demirhan and A. Alkhateeb, "Enabling cell-free massive mimo systems with wireless millimeter wave fronthaul," *IEEE Transactions on Wireless Communications*, vol. 21, p. 9482–9496, Nov. 2022.

[48] Q. Wu, S. Zhang, B. Zheng, C. You, and R. Zhang, "Intelligent reflecting surface-aided wireless communications: A tutorial," *IEEE Transactions on Communications*, vol. 69, no. 5, pp. 3313–3351, 2021.

[49] Q. Wu and R. Zhang, "Towards smart and reconfigurable environment: Intelligent reflecting surface aided wireless network," *arXiv.org*, 2019.

[50] X. Yuan, Y.-J. A. Zhang, Y. Shi, W. Yan, and H. Liu, "Reconfigurable-intelligent-surface empowered wireless communications: Challenges and opportunities," *IEEE wireless communications*, vol. 28, no. 2, pp. 136–143, 2021.

[51] F. C. Okogbaa, Q. Z. Ahmed, F. A. Khan, W. B. Abbas, F. Che, S. A. R. Zaidi, and T. Alade, "Design and application of intelligent reflecting surface (irs) for beyond 5g wireless networks: A review," *Sensors*, vol. 22, no. 7, 2022.

[52] A. Wolff, L. Franke, S. Klingel, J. Krieger, L. Mueller, R. Stemler, and M. Rahm, "Continuous beam steering with a varactor-based reconfigurable intelligent surface in the ka-band at 31 ghz," *Journal of applied physics*, vol. 134, no. 11, 2023.

[53] S. Hum, G. McFeetors, and M. Okoniewski, "Integrated mems reflectarray elements," vol. 626, pp. 1 – 6, 12 2006.

[54] C. Huang, A. Zappone, G. C. Alexandropoulos, M. Debbah, and C. Yuen, "Reconfigurable intelligent surfaces for energy efficiency in wireless communication," *IEEE transactions on wireless communications*, vol. 18, no. 8, pp. 4157–4170, 2019.

[55] Q. Wu and R. Zhang, "Intelligent reflecting surface enhanced wireless network: Joint active and passive beamforming design," in *2018 IEEE Global Communications Conference (GLOBECOM)*, pp. 1–6, IEEE, 2018.

[56] I. Nimnadini, A. Mezghani, and E. Hossain, "Low-overhead kronecker-based intelligent reflective surfaces for 5g and beyond," in *2024 IEEE 10th World Forum on Internet of Things (WF-IoT)*, pp. 382–387, 2024.

[57] E. Bjornson, O. Ozdogan, and E. G. Larsson, "Intelligent reflecting surface versus decode-and-forward: How large surfaces are needed to beat relaying?," *IEEE Wireless Communications Letters*, vol. 9, no. 2, pp. 244–248, 2020.

[58] T. Sharma, A. Chehri, and P. Fortier, "Reconfigurable intelligent surfaces for 5g and beyond wireless communications: A comprehensive survey," *Energies (Basel)*, vol. 14, no. 24, pp. 8219–, 2021.

[59] Q. Wu and R. Zhang, "Intelligent reflecting surface enhanced wireless network: Joint active and passive beamforming design," in *2018 IEEE Global Communications Conference (GLOBECOM)*, pp. 1–6, IEEE, 2018.

[60] R. W. Heath Jr and A. Lozano, *Foundations of MIMO Communication*. Cambridge: Cambridge University Press, 1 ed., 2018.

[61] D. Wijekoon, A. Mezghani, and E. Hossain, "Phase shifter optimization in ris-aided mimo systems under multiple reflections," *IEEE transactions on wireless communications*, pp. 1–1, 2024.

[62] H. Ur Rehman, F. Bellili, A. Mezghani, and E. Hossain, "Joint active and passive beamforming design for irs-assisted multi-user mimo systems: A vamp-based approach," *IEEE transactions on communications*, vol. 69, no. 10, pp. 6734–6749, 2021.

[63] A. Mezghani, F. Bellili, and E. Hossain, "Nonlocal reconfigurable intelligent surfaces for wireless communication: Modeling and physical layer aspects," 2022.

[64] S. P. Boyd and L. Vandenberghe, *Convex Optimization*. Cambridge, UK: Cambridge University Press, 2004.